ANALYSIS OF PASSIVE RADIOMETRIC SATELLITE OBSERVATIONS OF SNOW AND ICE

by

Stanley Richard Rotman

Submitted in Partial Fulfillment

of the Requirements for the

Degree of Bachelor of Science

at the

MASSACHUSETTS INSTITUTE OF TECHNOLOGY

December, 1978

(i.e. June, 1979)

Signature of Author..
Department of Electrical Engineering
and Computer Science, 1978

Certified by..
Thesis Supervisor

Accepted by..
Chairman, Departmental Committee on Theses

ACKNOWLEDGMENTS

This thesis would have been impossible without the assistance of a great number of people. First and foremost, I offer my thanks to Dr. D.H. Staelin for the time and assistance he has put in as my thesis advisor and as my supervisor on this work.

I must also thank Mr. A. D. Fisher who suggested many of the steps this thesis has taken and has supplied most of the clustering programs used. Much of the preliminary work done on this project is his.

Additional thanks must be given to Leung Tsang for his help in reading this thesis and to Jeremy Nussbaum for providing both curve fitting programs and a friendly office (outside of my own) in which to discuss my research. A great deal of programming time was furnished by SIPB (Student Information Programming Board).

DEDICATION

To My Parents

to whom scattering, snow and Zwally
have become household words.

TABLE OF CONTENTS

	Page
Title Page	1
Acknowledgments	2
Dedication	3
Abstract	9
Chapter 1 -- Introduction	10
Chapter 2 -- The Satellite and the Groundtruth	13
Chapter 3 -- Data Classification	21
Chapter 4 -- Experimental Clustering Results	29
Chapter 5 -- Theory of Snow Scattering	45
Chapter 6 -- Experimental Results for Snow Accumulation	62
Chapter 7 -- Effects of the Thermal Gradient	78
Chapter 8 -- Summary and Conclusions	94

LIST OF MAPS

	Page
Map 1 -- Ten Meter Temperature for Antarctica	15
Map 2 -- Ten Meter Temperature for Greenland	16
Map 3 -- Accumulation Rate Map for Antarctica (Circular Projection)	19
Map 4 -- Accumulation Rate Map for Greenland (Circular Projection)	20
Map 5 -- Clustered Map for Antarctica (33 clusters)	30
Map 6 -- Clustered Map for Antarctica (10 clusters)	31
Map 7 -- Clustered Map for Antarctica (6 clusters)	32
Map 8 -- Clustered Map for Arctic (40 clusters)	34
Map 9 -- Orthogonal Components Clustered Map for Antarctica	40
Map 10 -- September K-nearest Neighbors Map for Antarctica	42
Map 11 -- November K-nearest Neighbors Map for Antarctica	43
Map 12 -- January K-nearest Neighbors Map for Antarctica	44
Map 13 -- Accumulation Rate Map for Antarctica (Elliptical Projection)	66
Map 14 -- 31 GHz Accumulation Rate Map for Antarctica	67
Map 15 -- Accumulation Rate Map for Greenland (Elliptical Projection)	69
Map 16 -- 31 GHz Accumulation Rate Map for Greenland	70

LIST OF MAPS (CONT.)

	Page
Map 17 -- 22 GHz Accumulation Rate Map for Antarctica	72
Map 18 -- 22 GHz Accumulation Rate Map for Greenland	74
Map 19 -- Composite Accumulation Rate Map for Antarctica	76
Map 20 -- Composite Accumulation Rate Map for Greenland	77
Map 21 -- Thermal Gradient for Antarctica	91
Map 22 -- Thermal Gradient for Greenland	92

LIST OF FIGURES

Page

Figure 1 -- Sample Complete-Link Dendrogram 23

Figure 2 -- Sample Single-Link Dendrogram 23

Figure 3 -- Sample Linear Dendrogram 26

Figure 4 -- Sample Non-Linear Dendrogram 27

Figure 5 -- Microwave Signatures of Firn 36

Figure 6 -- Microwave Signatures of Ice and Water 37

Figure 7 -- The Z Function 49

Figure 8 -- Least Squares Fit for K_{10} and K_{11} 64

Figure 9 -- A Model Temperature Gradient 79

Figure 10 -- T_{b22}-T_{b31} for Antarctica 80

Figure 11 -- T_{b22}-T_{b31} for Greenland 82

LIST OF TABLES

	Page
Table 1 -- Absorption Coefficients	52
Table 2 -- Predicted 22 GHz Temperatures	60
Table 3 -- Data for Least Squares Fit for K_{10} and K_{11}	63
Table 4 -- Latitude Effect on Temperature Swing	87

ANALYSIS OF PASSIVE RADIOMETRIC SATELLITE OBSERVATIONS OF SNOW AND ICE

BY

Stanley Richard Rotman

Submitted to the Department of Electrical Engineering
and Computer Science

on December 1, 1978 in partial fulfillment of the requirements

for the Degree of Bachelor of Science

ABSTRACT

The Nimbus-6 satellite's SCAnning Microwave Spectrometer (SCAMS) observed the earth's surface radiometrically at nadir and six off-center angles with two frequencies (22.2 and 31.6 GHz.) Previous theoretical work indicated that physical parameters of the ground surface should be discernable from these radiometric soundings.

Automatic classification methods based on pattern recognition were applied to the data; geographical classes were generated representing sea-ice (ice age subclasses), firn (accumulation rate subclasses), water, and fresh snow over ice. Characteristic SCAMS signatures produced by the various snow and ice types were also identified.

Further analysis of the data over Greenland and Antarctica at three distinct times of the year indicated the quantitative ability to detect long-term accumulation rates and changes in the temperature profile of the snow. A semi-empirical method has been devised to process the observations and invert for some of the physical parameters of the snow. Accumulation maps of Antarctica and Greenland as predicted by this data are included.

Thesis Supervisor: David H. Staelin

Title: Professor of Electrical Engineering

CHAPTER I -- INTRODUCTION

The microwave brightness temperature of an object, T_b, is defined as the temperature of a blackbody which emits the same amount of radiation as the observed object. The Rayleigh-Jeans approximation can be employed at microwave frequencies:

$$T_b \approx \frac{2 K_B T}{\lambda^2} W(T) \qquad (1-1)$$

where W(T) (watt m^{-2} rad^{-2} hz^{-1}) is the radiance of the blackbody at a specific temperature, T is the physical temperature, K_B is Boltzmann's constant and λ is the wavelength of the radiation. Emissivity is defined as the ratio of the brightness temperature to the physical temperature of an object.

I have applied automatic pattern recognition techniques to satellite-observed brightness temperatures at 22.2 and 31.6 GHz. covering the Arctic (70° - 80°N) and Antarctic (70° - 80°S) regions. This both enables automatic class identification (without predetermining the possible classes) and provides an efficient manner to study brightness temperature variation with angles.

Furthermore, radiometric observations of snow at microwave frequencies have shown low values of emissivity (0.65-0.9) over the firn of Greenland and Antarctica. (Firn is hard-packed snow which has accumulated over terrain for many years.) Absorption by the snow and the emissivity of the air-snow boundary alone do not properly explain these results unless volume scattering of radiation by the snow medium is included.[1] Models explaining the scattering properties of the snow have been developed. Chang et al.[2] and Zwally[3] modeled the snow as spherical crystals and calculated the Rayleigh and Mie scattering. Fisher[4,5] and Tsang et al.[6,7] have analyzed scattering based on one-dimensional (laminar) and three-dimensional statistically stationary and nonstationary refractive index fluctuations. Since the scattering and absorption of the snow are functions of its temperature, density, and particle size, the physical parameters of the snow should be observable. Zwally[3] correlated snow particle size with observed emissivity and used these data to calculate the accumulation rate at a few select areas.

My method of inverting for accumulation attempts to further Zwally's work; using a linear statistical process, it finds the accumulation rate from the observed emissivity and groundtruth. Undetermined coefficients in a theoretical equation, relating emissivity to snow accumulation and temperature, are empirically fitted to groundtruth data (in a least-squares sense.) I then generate my own accumulation maps on a second pass using these coefficients, the observed emissivity, and the ten meter temperature. These derived maps will on the average resemble the groundtruth accumulation maps which served as the data base, but may differ in specific areas. The change in brightness temperature between seasons has also been analyzed; using 22.2 and 31.6 GHz. data, the effects of variations of temperature with depth in snow can be observed.

CHAPTER 2 -- THE SATELLITE AND THE GROUNDTRUTH

The Scanning Microwave Spectrometer, on board the Nimbus-6 satellite, continuously maps the earth at 22.2, 31.6, 52.8, 53.8, and 55.4 GHz.[8] The latter three frequencies are used to probe the atmospheric temperature profile.[9] The 22.2 and 31.6 GHz. frequencies map the earth's surface with a resolution of approximately 150 km. by 150 km. at seven angles relative to the nadir: 0.0°, 7.2°, 14.4°, 21.6°, 28.8°, 36.0°, and 43.3°. The polarization is dependent on the scan angle θ of the satellite such that $T_b=T_h \cos^2\theta + T_v \sin^2\theta$ where T_h and T_v are the brightness temperatures due to the horizontally and vertically polarized radiation components respectively.

Nine hundred vector datasets for both the Arctic (70° - 80°N) and Antarctic regions (70° - 80°S) at three seasons were collected. Each vector has fourteen components (nadir and the six angular brightness temperatures at 22.2 and 31.6 GHz); the latitude and longitude of each point are used as identifiers. Vectors with missing components were excluded from the automatic pattern recognition processing; approximately seven hundred valid vectors remain. Since the satellite covers only a limited part of the globe every day, weekly averages were used.

The groundtruth data for surface temperature and snow accumulation for Antarctica and Greenland areas were obtained from references 10 and 11. The mean surface temperature maps (Maps 1 and 2) are reported to be very reliable in contrast to the accumulation maps.[10] The temperature at ten meters depth, designated here as T_{10}, is assumed to be equal to the mean seasonal surface temperature. It is predicted that the ten meter temperature is within 1.5°K of the mean surface temperature at any time.[10] In what is termed the "coreless" effect,[12] the mean temperature is far below the middle of the yearly warm to cold temperature extremes caused by the long, constantly cold, sunless winter.

In order to effectively analyze microwave radiometric data, an accurate description of the snow's temperature profile is required. Bull[10] reports that the temperature at any depth is approximately exponential, i.e. of the form

$$T(z)= T_{10} + T_1 \exp(-fz) \qquad (2-1)$$

where T_{10} is the ten meter temperature, f is the decay constant, and T_1 is the difference between T_{10} and the surface temperature at the time of observation. However, it is clear that this is only an approximation; better fits have

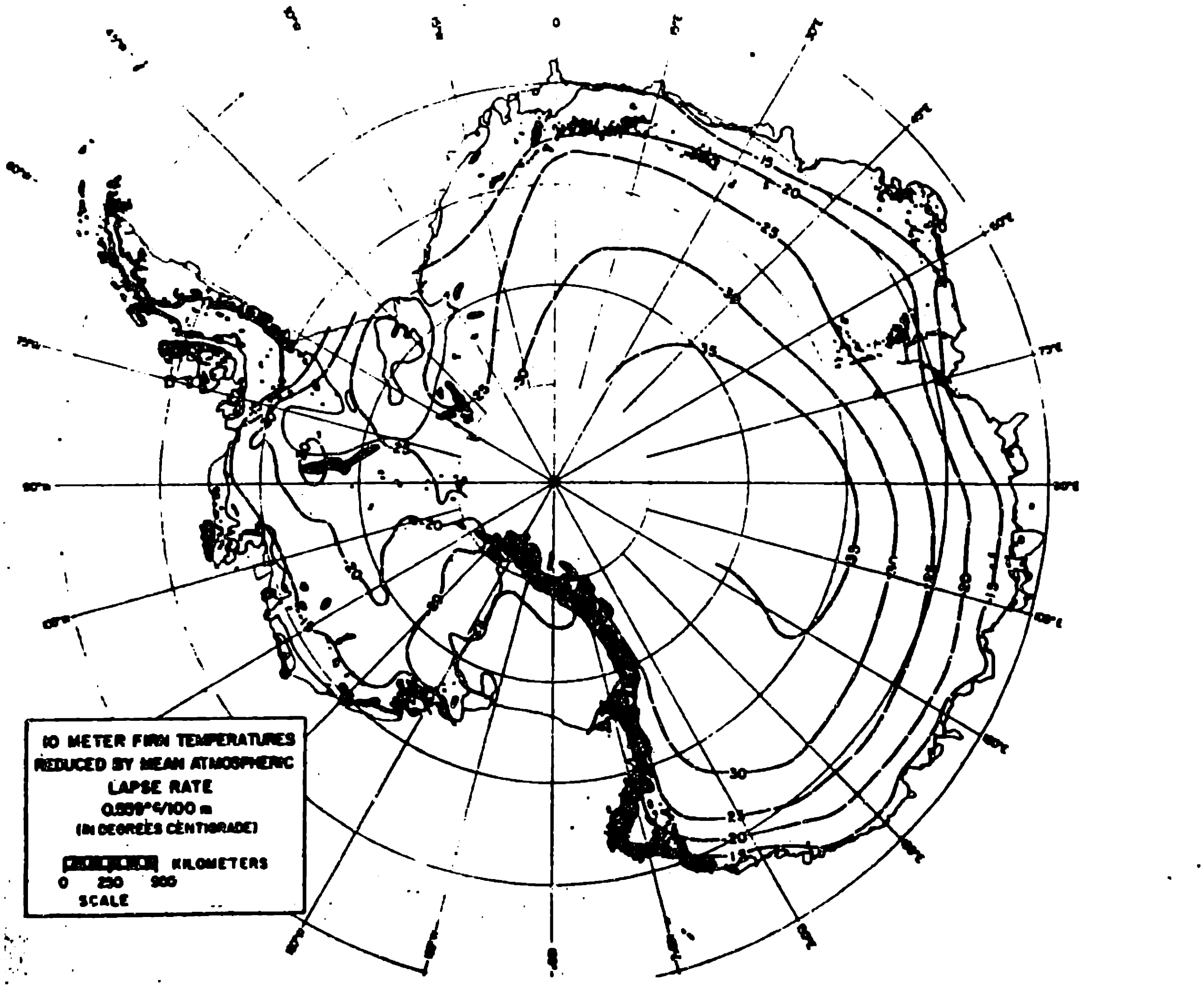

Map 1: Ten meter temperature map for Antarctica taken from Bentley et al.[10]

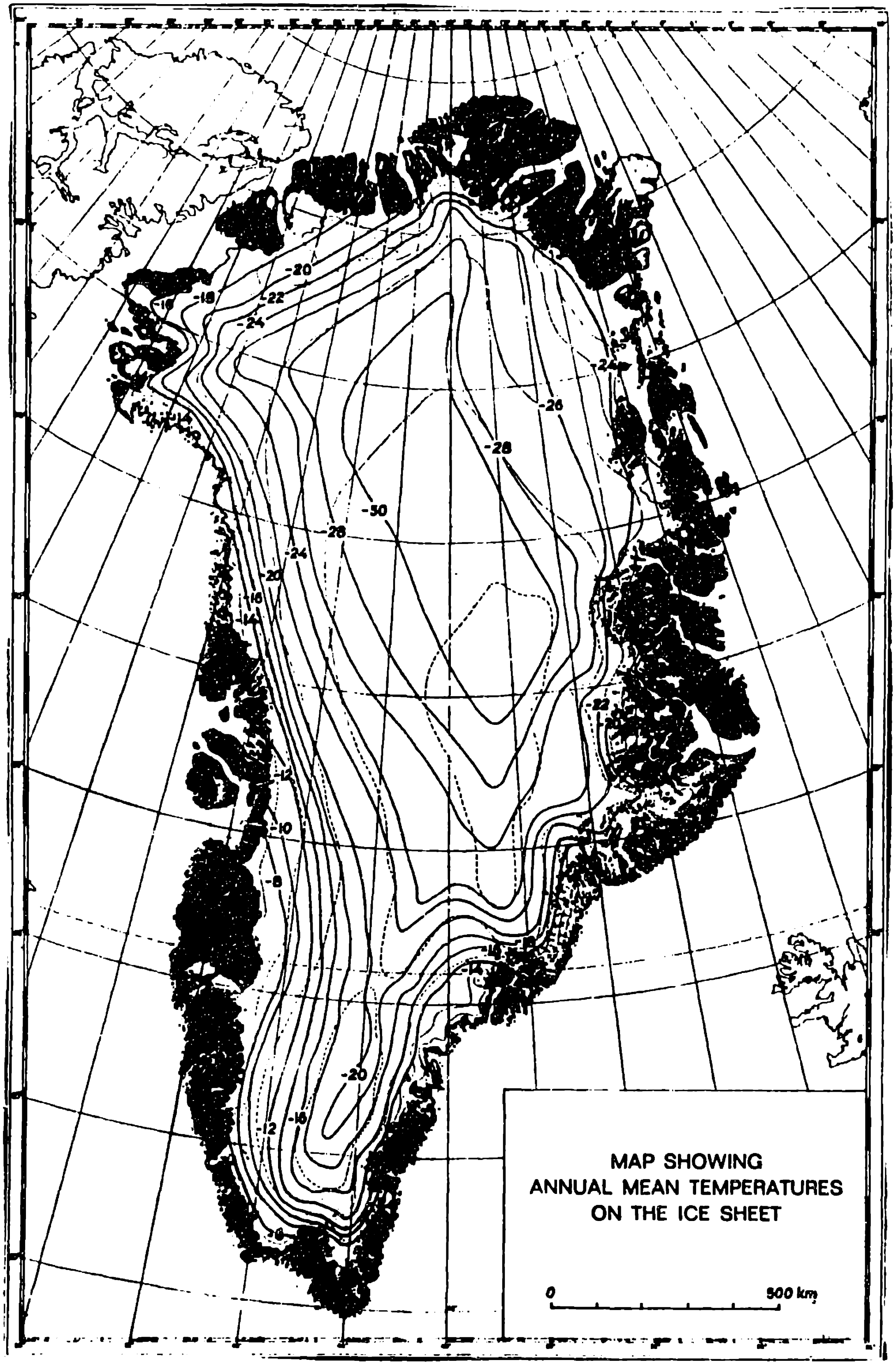

Map 2: Ten meter temperature map for Greenland.[11]
(Broken lines represent constant altitude contours in Greenland).

have been obtained with a semi-empirical thermal model[3] which predicts that

$$T(z) = T_{10} + T_1' \cos(a_1 z - a_2 t + a_3) \cdot \exp(-fz) \qquad (2\text{-}2)$$

where T_1' is the maximum seasonal change, a_1, a_2, and a_3 are constants determined by the nature of the snow, and t is the time of year; a period of one year is represented by t equal to $\frac{2\pi}{a_2}$. Higher harmonic terms, beyond the cosine dependence of equation 2-2, have been observed to propagate in layered media, such as lunar dust,[13] which have related electrical characteristics similar to snow. In my work, I have assumed that the period of November 20-30 represents a "constant" temperature profile (i.e. $T_1 = 0$) and that January 20-30 and September 20-30 are the times when T_1 is either a maximum or a minimum and the exponential profile (equation 2-1) is a good approximation. In Chapter 7, I shall show that the difference in brightness temperature in November between 22.2 and 31.6 GHz. frequencies is largely due to these temperature gradients in the snow.

Snow accumulation maps are more difficult to generate and less reliable than those for temperature profiles. A variety of methods have been found useful, including measurement of snow precipitation with gauges, measurement of snow accumulation using stakes, and isotope studies.[14] We will use Maps 3 and 4 as our groundtruth accumulation contours.

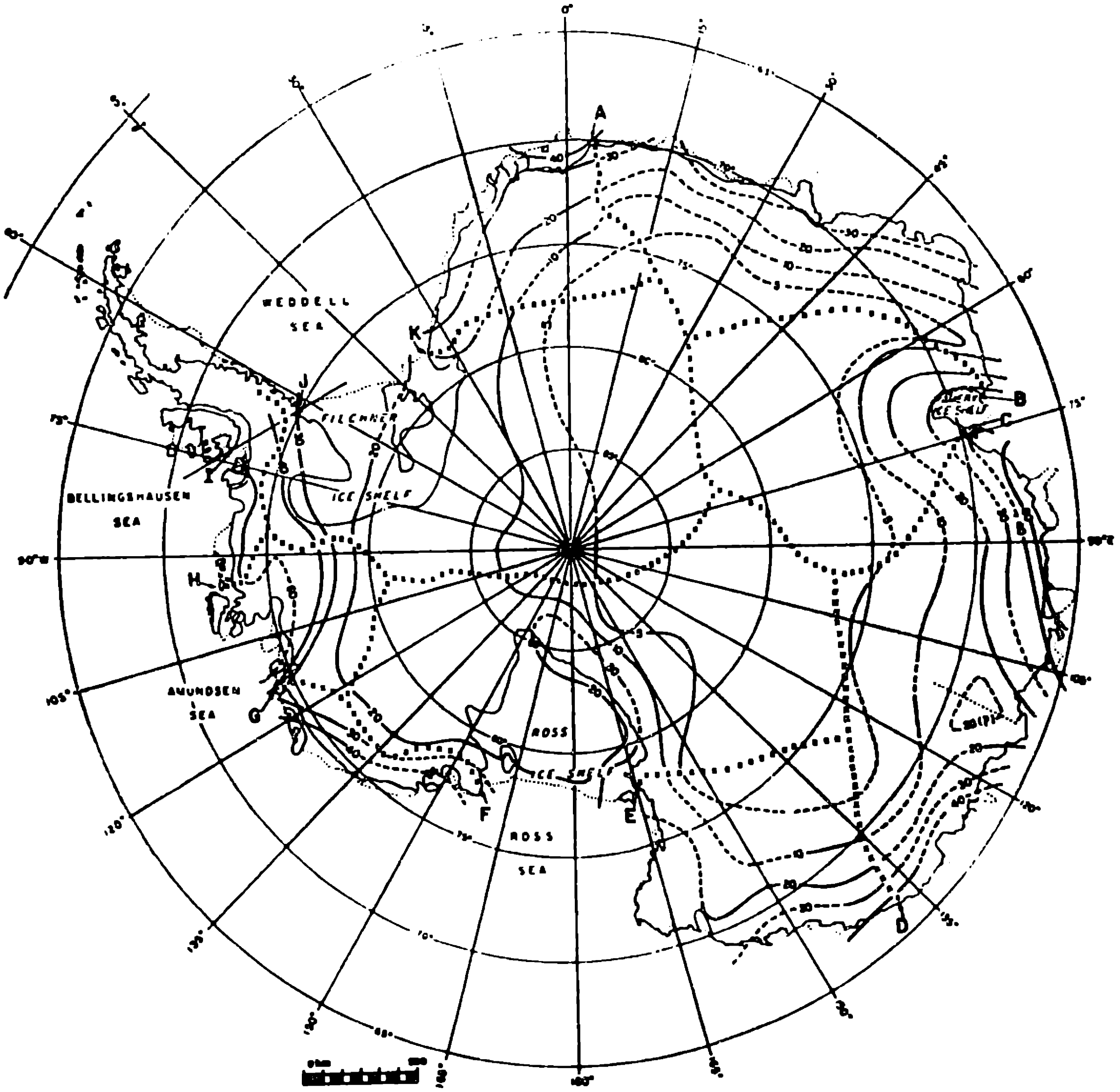

Map 3: Accumulation rate map for Antarctica similar to that of Bentley et al[10] (Broken lines are fault lines for Antarctica and should be ignored).

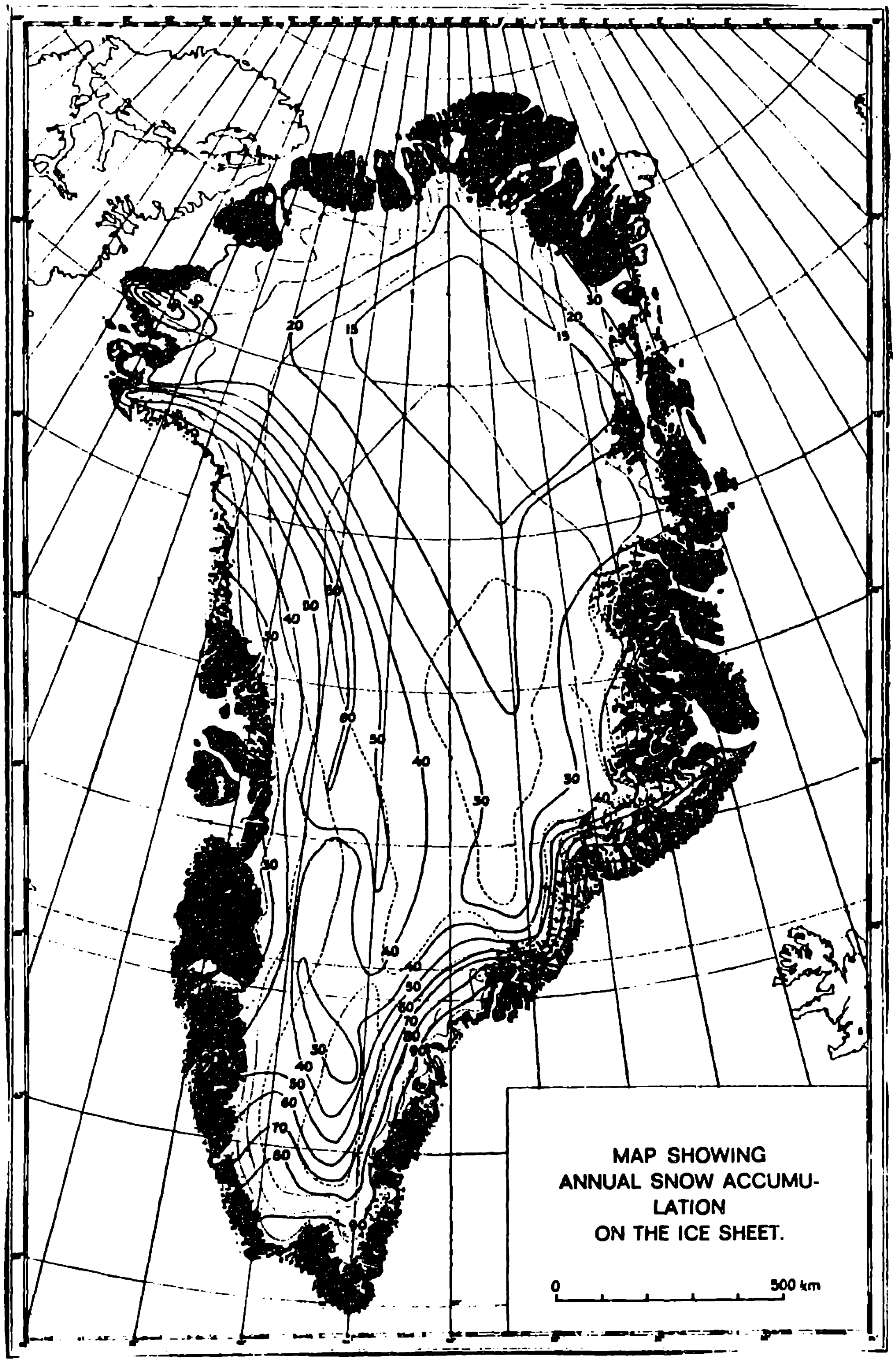

Map 4: Accumulation rate map for Greenland. Accumulation rates are given in units of gm/cm^2-year. (Broken lines represent constant altitude contours in Greenland.)

CHAPTER 3 -- DATA CLASSIFICATION

Pattern recognition has an advantage over other means of processing microwave data since a theoretical model is not needed.[16] Our method of clustering uses a hierarchical approach; similar vectors are automatically grouped together into classes.[15] There is no guarantee that the resulting classes will be meaningful or will correspond to physical parameters (after all, even vectors with random noise would cluster.) However, our results can be judged by two criteria; first, if we have meaningful clusters, geographically connected areas should be grouped in the same class since neighboring areas will often have the same physical characteristics. Second, since the brightness temperatures observed are, at least partially, functions of accumulation and temperature, we would expect some classes to follow contours of constant accumulation and temperature.

Two separate processes occur in the automatic pattern recognition procedure: the clustering of the data and the displaying of the data in the form of a dendrogram (tree-like graph.) When the clustering process first begins, each vector is treated as a one-member cluster. The Euclidian distance between each vector and every other vector in the dataset is computed and stored. Then, the distance threshold for which two clusters are combined, designated as the variable "thresh", increases monotonically to form new clusters. Many options exist for computing the distances of vectors from a newly formed cluster; we have used two techniques: single-link and complete-link clustering. Complete-link clustering assigns as a measure for the newly formed cluster the furthest distance of any of the new cluster's vectors to each of the other vectors in the dataset while single-link clustering uses the closest distance.

The clustering procedure will now be demonstrated with reference to the dendrograms of Figures 1 and 2. For example, imagine four vectors located in two dimensional space: vector 1 (referred to as V1) at (0,0), vector 2 (V2) at (0,1), vector 3 (V3) at (0,3), and vector 4 (V4) at (0,5.5). The clustering program computes the distance for both single and complete link clustering as follows:

	V1	V2	V3
V2	1.0		
V3	3.0	2.0	
V4	5.5	4.5	2.5

DENDROGRAMS

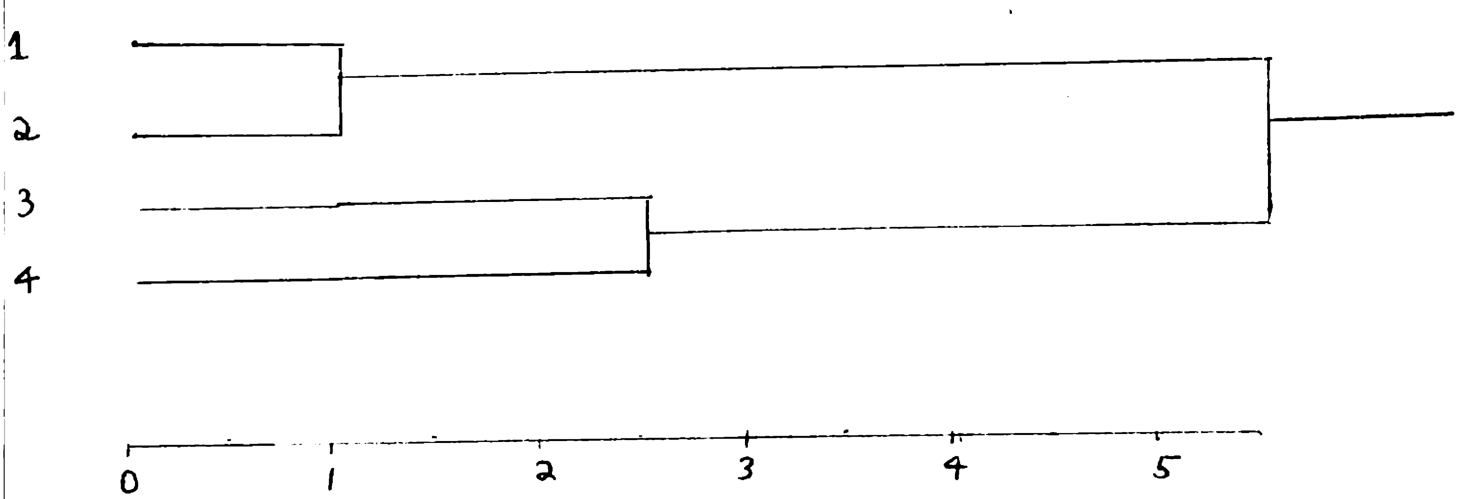

Figure 1: A sample dendrogram for complete-link clustering.

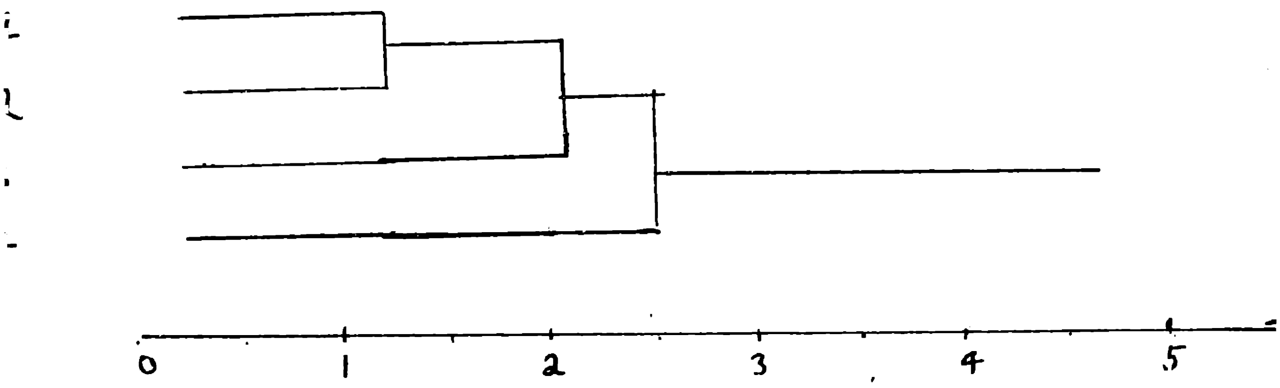

Figure 2: A sample dendrogram for single-link clustering.

The threshold is now increased monotonically. For complete clustering (Fig.-1), V1 and V2 combine when thresh = 1. With the new vector, called V1-2 in our notation, the new distance matrix is formed as follows:

	V1-2	V3
V3	3.0	
V4	5.5	2.5

Note that V1, now one of the two components of V1-2, has determined the distance of V1-2 from V3 and V4. V3 and V4 combine when thresh equals 2.5; then V1-2 and V3-4 combine when thresh equals 5.5.

For single-link clustering (Fig.-2), V2 and V3 again combine when thresh equals 1. However the new distances are as follows:

	V1-2	V3
V3	2.0	
V4	4.5	2.5

V1-2 will combine with V3 when thresh equals 2 while V1-2-3 and V4 combine when thresh equals 2.5.

The tendency of large clusters to attract stragglers when using single-link clustering is called chaining. Complete clustering will tend to form "convex" clusters (in our fourteen-dimensional space) while single-link clustering will allow "bridging" between two distinct clusters. The threshold continues to rise until all vectors in the dataset have been collected into one cluster.

A dendrogram which displays the nine hundred vectors and the states of the clusters for discrete values of threshold is formed to present the results. Two types of dendrograms are possible. A linear dendrogram computes the maximum threshold needed to gather all the vectors into one group and displays these states at equal intervals between zero and the maximum threshold. (For example, if the maximum threshold needed to group all the vectors into one cluster was two hundred and fifty and twenty five equal intervals were used, the dendrogram will display the state of the clusters at thresh = 10, 20, 30... 250.) A non-linear dendrogram enables the user to input non-uniformly spaced values of the threshold at which he wishes to see the state of the clusters. Sample output dendrograms are shown in Figures 3 and 4.

Once the clusters have been formed, four processing methods were used. First, the groups of clusters at different levels of thresh were replotted into geographical maps.

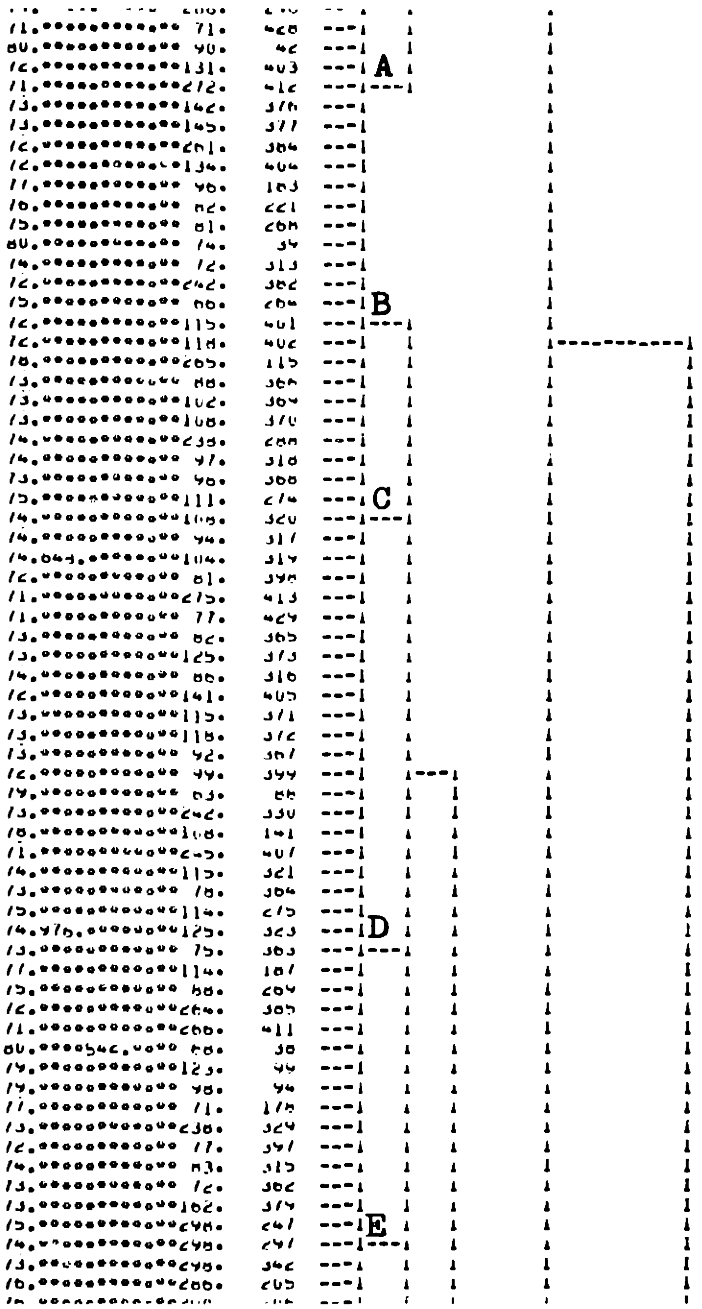

Figure 3: A linear dendrogram. Letters on dendrogram correspond to identical positions in Figure 4.

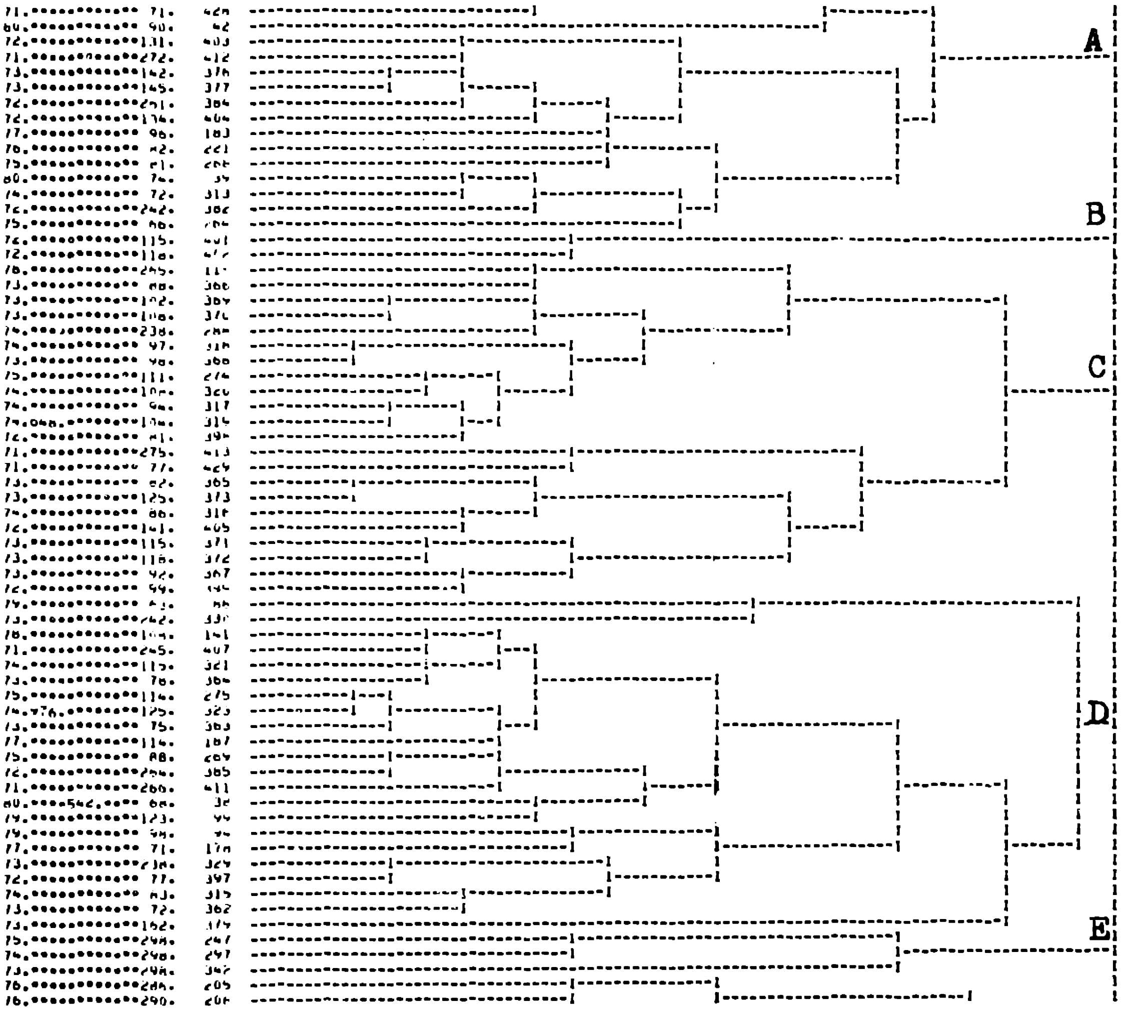

Figure 4: A non-linear expanded dendrogram. Letters on dendrogram correspond to identical positions in Figure 3.

Contour plots were made for Antarctica and Greenland. Second, the mean values and the variances of the brightness temperatures were plotted as a function of angle for each cluster at both 31.6 and 22.2 GHz. Third, a K-nearest neighbors routine was used;[16] this program takes vectors which are calculated from new experimental data and compares them with sample vectors in predetermined classes. The K most similar sample vectors to the experimental vector are found; the experimental vector is then assigned to the class which contains the greatest number of these K vectors. For example, if we assign arbitrarily K = 5, and if the closest vectors to the experimental vectors are in class 1, class 2, class 1, class 2, and class 2 respectively in order of increasing distance from the experimental vector, then the experimental vector will be assigned to class 2. (If K = 3, the vector would have been assigned to class 1.) Fourth, a rotation program using the Karhunen-Loève method was used.[17] The rotation program computes the correlation matrix for the fourteen-dimensional vector space and rotates the coordinate system to point along the orthogonal trends in the dataset. The significant trends in the data can be discriminated from repetitive and non-useful information. This method can be used to reduce a fourteen-dimensional vector space to a more manageable size.

CHAPTER 4 -- EXPERIMENTAL CLUSTERING RESULTS

Excellent results were obtained for the clustering of the brightness temperature data. Distinct geographical clusters appeared for the Arctic and Antarctic regions for three seasons with both complete- and single-link clustering. The maps analyzed were produced by complete clustering.

Maps 5, 6, and 7 show three levels of clustering for Antarctica in September, 1975. Even though Map 5 has thirty-three clusters (a high number of classes), interesting geographical features are visible. The band structure of the clusters is characteristic of the accumulation contours. Low accumulation clusters formed in the regions: 30°E, 77° to 79°S and 140°E, 77° to 79°S; other regions of higher accumulation levels (symbols 4, 5, 7, and 8) are also visible on the map. The clusters in order of increasing accumulation rate are symbols B, C, 9, A, 0, 1, 2, 3, 4, 7, 8, 5, and 6. New sea ice at around 30°W, 75° to 79°S is represented by clusters O and P (also found at 150°W.) The area of low accumulation at approximately 120°W stands out distinctly.

Reducing the number of classes to ten helps clarify the clusters, as seen in Map 6. Clusters 4, 0, 1, 3, 2, and 6 represent, in order of increasing accumulation rate, the

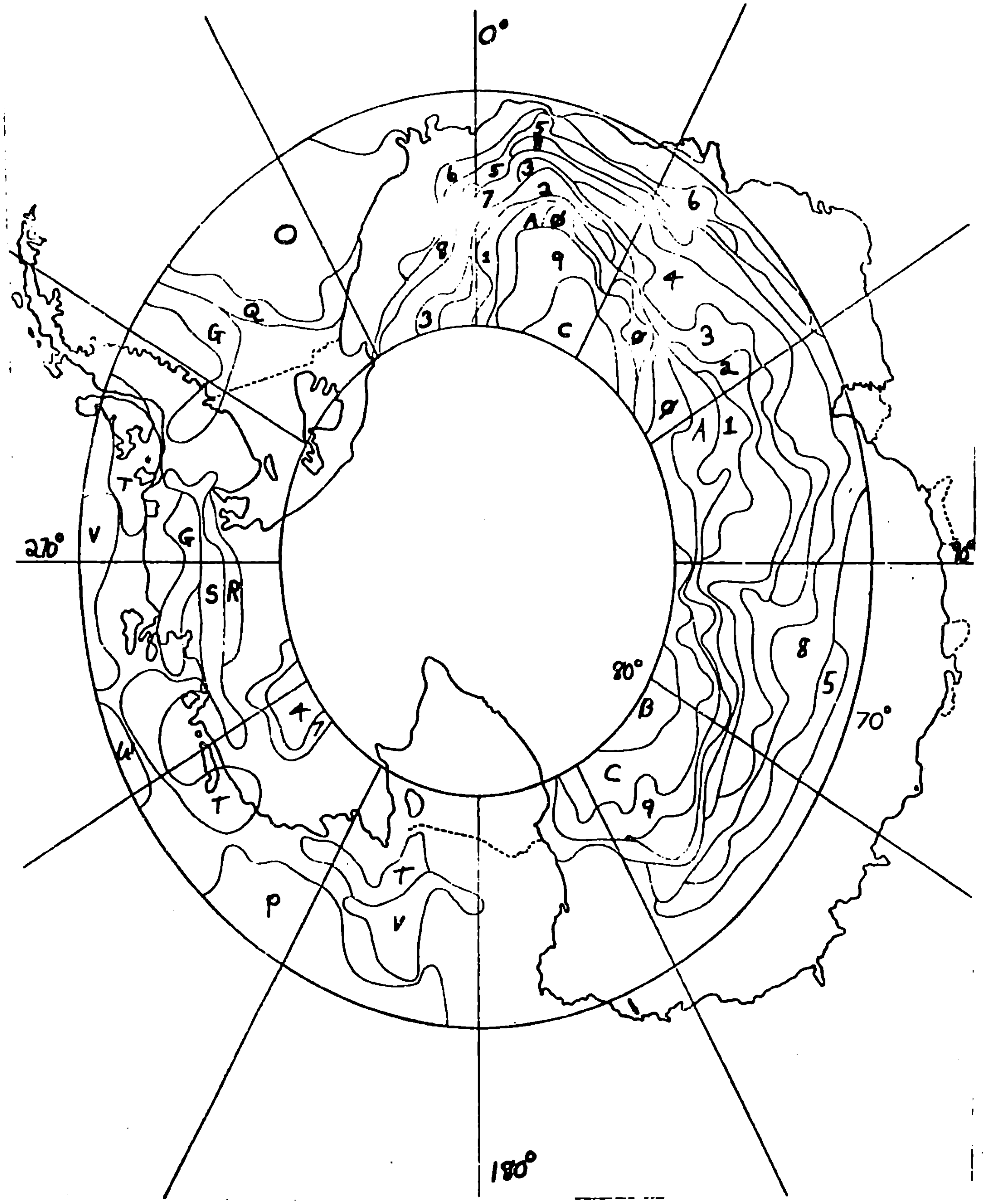

Map 5: Clustered map for Antarctica in September using 33 clusters. Symbols are arbitrary. (Ø and O are distinct clusters). Not all clusters are shown.

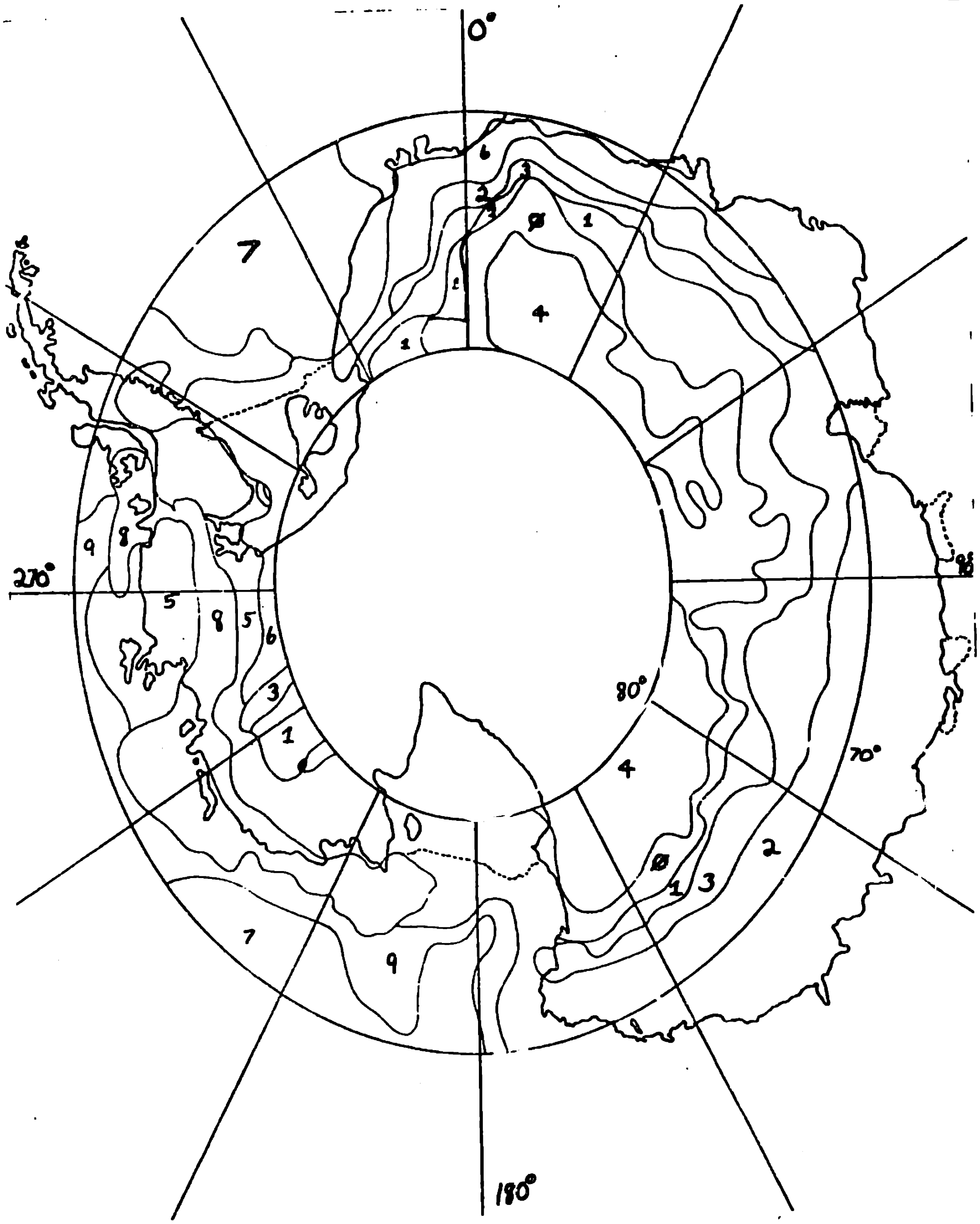

Map 6: Clustered map for Antarctica in September for 10 clusters. Symbols for the different clusters are arbitrary.

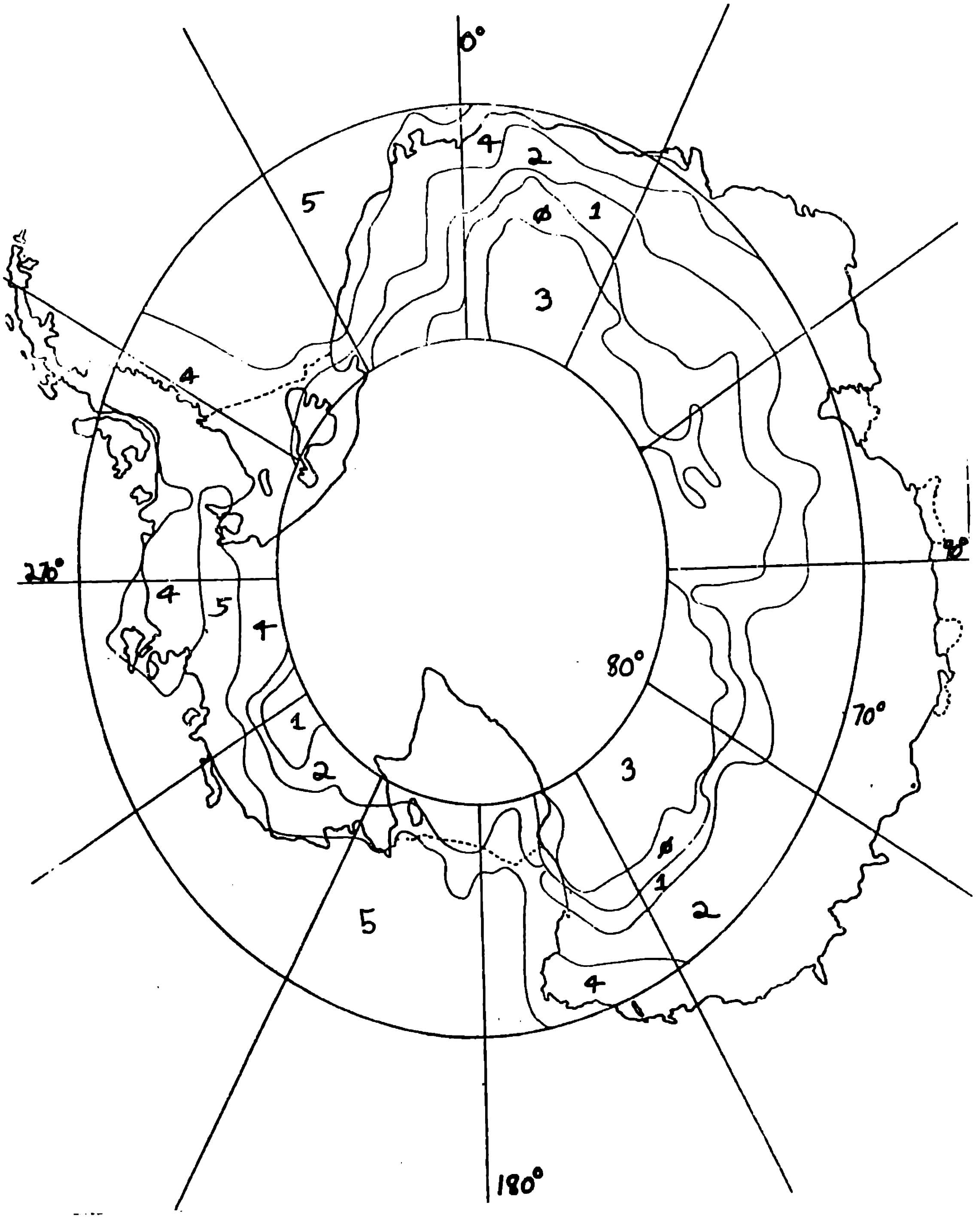

Map 7: Clustered map of Antarctica for September with 6 clusters. Symbols are arbitrary for the clusters.

areas of firn in Eastern Antarctica. Cluster 5 is mostly firn in Western Antarctica with a slight overlap onto sea ice. I will show later in this chapter that firn has a lower brightness temperature than sea ice. However, as the accumulation rate increases in Western Antarctica, the brightness temperature increases and the firn looks more and more like sea ice. In Map 6, sea ice is shown by clusters 7, 9, and 8 in order of increasing age.

Map 7 shows the entire region using only six clusters. The firn in the Eastern area of Antarctica is represented by five clusters, symbols 3, 0, 1, 2, and 4, in order of increasing accumulation rate. All of the sea ice (and unfortunately, a small part of Western Antarctica) is grouped in Cluster 5. Since the resolution is only 150 km. by 150 km., boundary areas, where the radiometer sees a mixture of both ice and firn, are poorly classified (as can be seen near the coast of Antarctica at approximately 165°E.)

In Map 8, the Arctic region is clustered and processed for September 1975, the summer in this area. The clustering contours in Greenland can be seen to follow the accumulation contours. Clusters 5, I, H, and E are representative of the permanent ice pack (as outlined from groundtruth by the

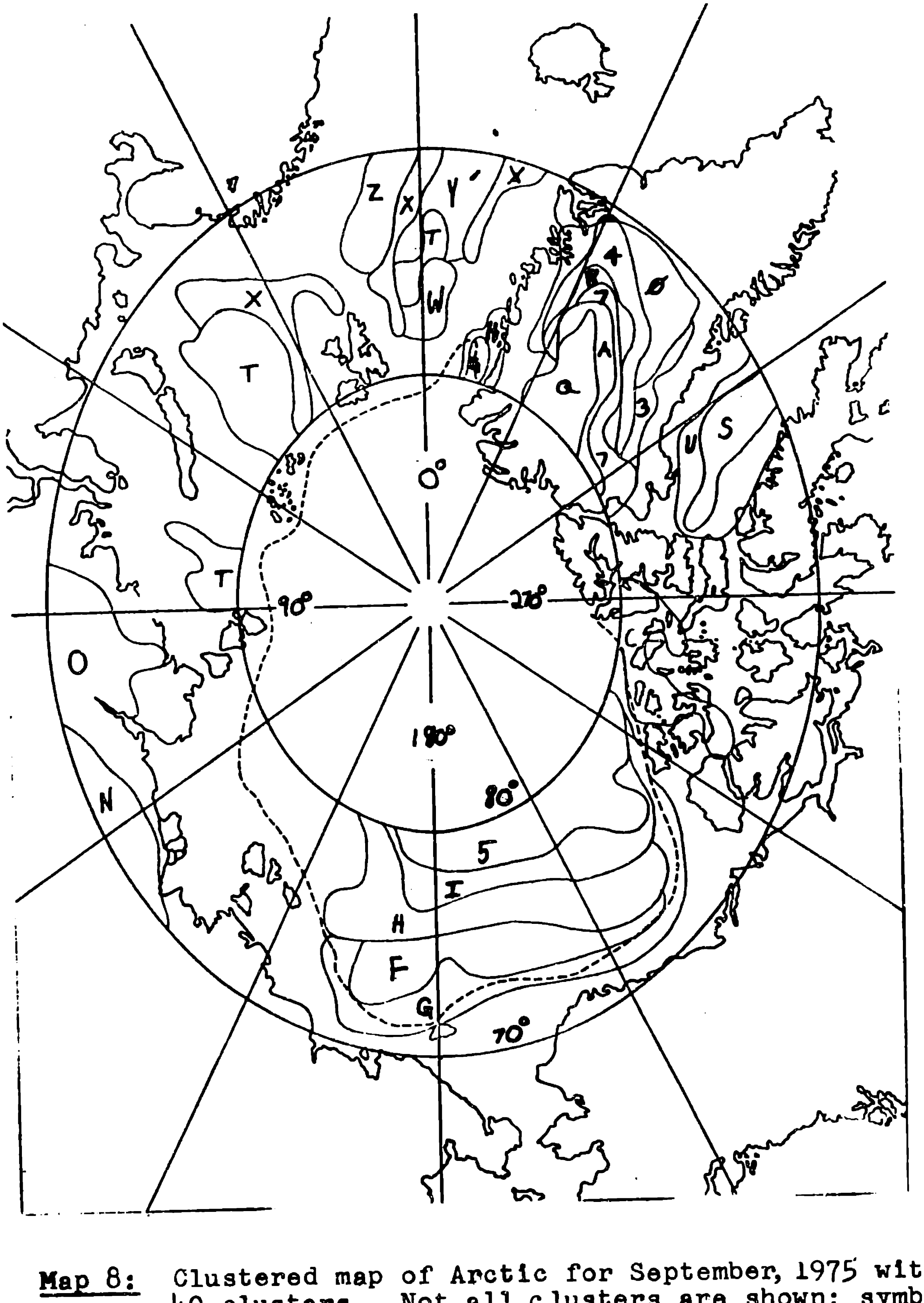

Map 8: Clustered map of Arctic for September, 1975 with 40 clusters. Not all clusters are shown; symbols for different clusters are arbitrary.

broken line.) Permanent ice can also be found to the east of Greenland, shown by the presence of data points grouped into clusters G and H. The open expanses of water, indicated by the low brightness temperatures of clusters S, Z, and T, and bare ground, clusters N and O in Siberia, are also visible. As the seasons progress, the microwave signatures show the freezing of the open water areas around 45°E and the covering of Siberia with snow.

The mean values of the brightness temperatures for each cluster are next plotted as a function of angle. Typical signatures can be seen in Figures 5 and 6. Observations of the surface show the following general order of increasing brightness temperatures: (a) water, (b) firn (brightness temperature increasing with accumulation), (c) multi-year sea ice (brightness temperature decreasing with age), (d) snow over land, and (e) first-year ice.

The shapes of the curves are very informative although separate polarization information is lacking. As discussed later, scattering within the bulk of the snow has a large effect on the brightness temperature (the larger the scattering, the lower the brightness temperature.) Since the multi-year sea ice's brightness temperature decreases with increased angle from the nadir, the scattering must be

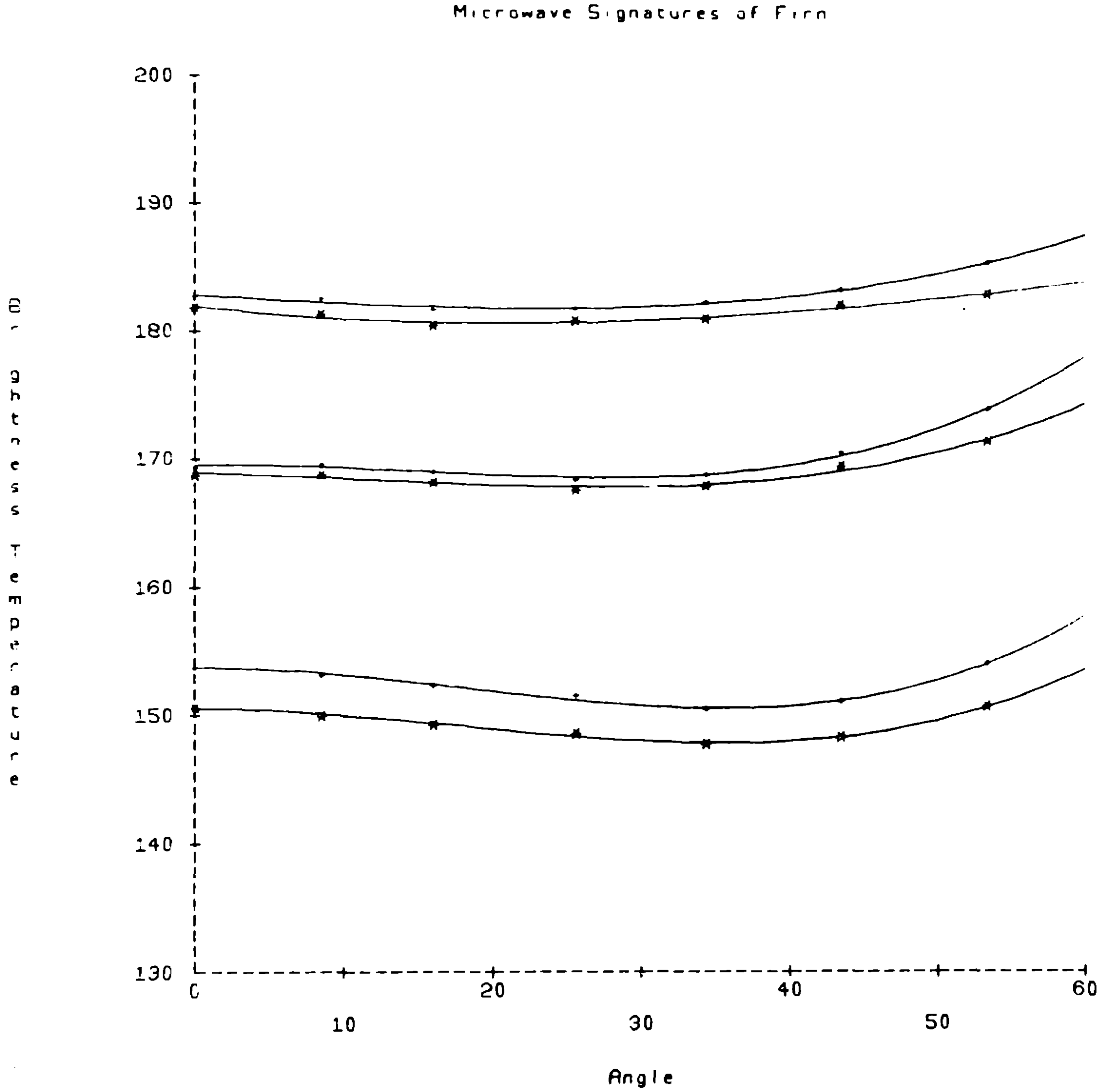

Figure 5: Typical microwave signatures of firn from Antarctica in September. "+" and "*" signify 22 and 31 GHz observations respectively. The three curves are high, medium, and low accumulation areas in Antarctica (in order of decreasing brightness temperature).

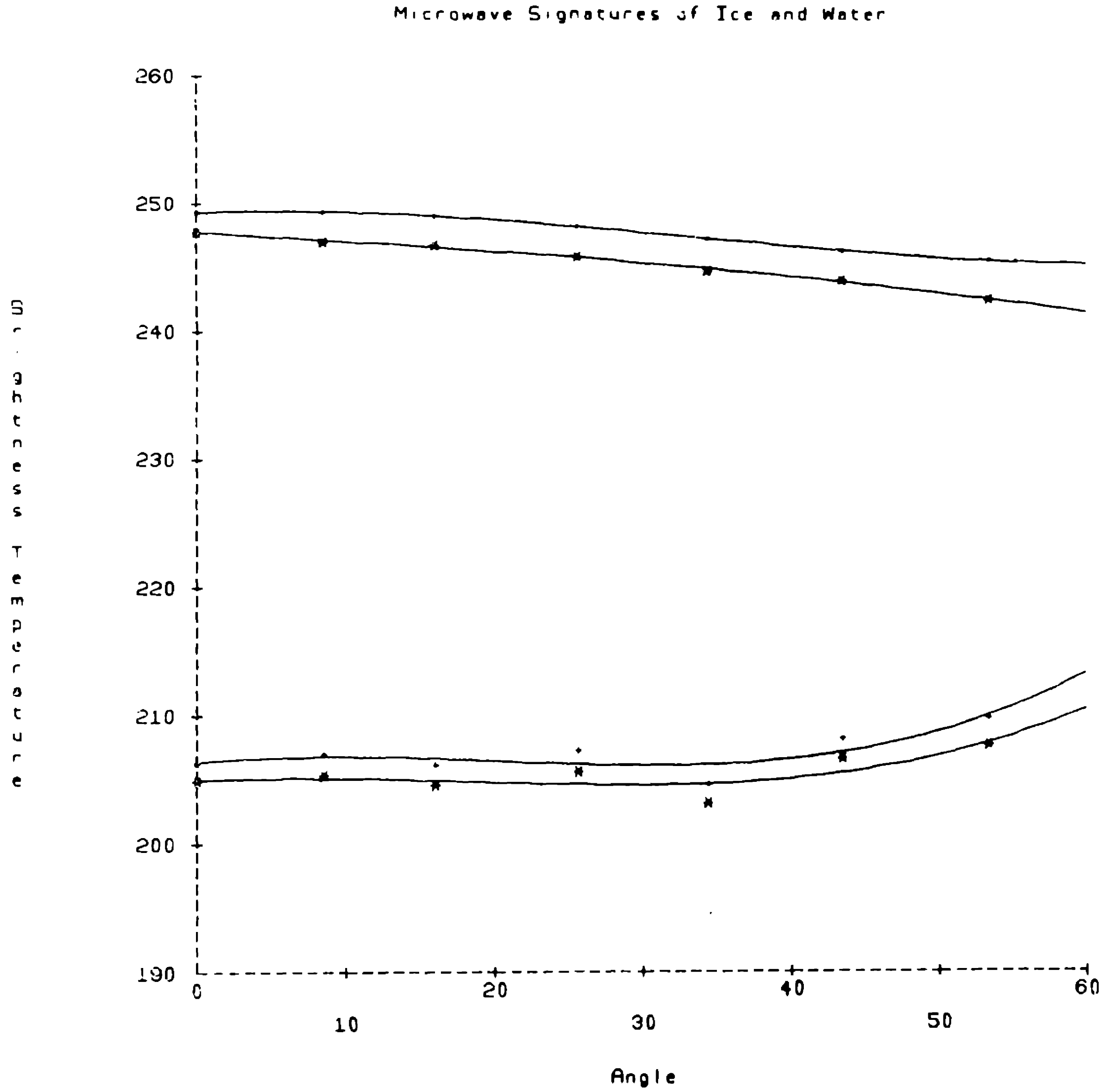

<u>Figure 6:</u> Typical microwave signatures of ice and water from Arctic region in September. Curves at ≈ 250° are new sea ice; curves at ≈ 210° are new sea ice mixed with water. "+" and "*" signify 22 and 31 GHz observations respectively.

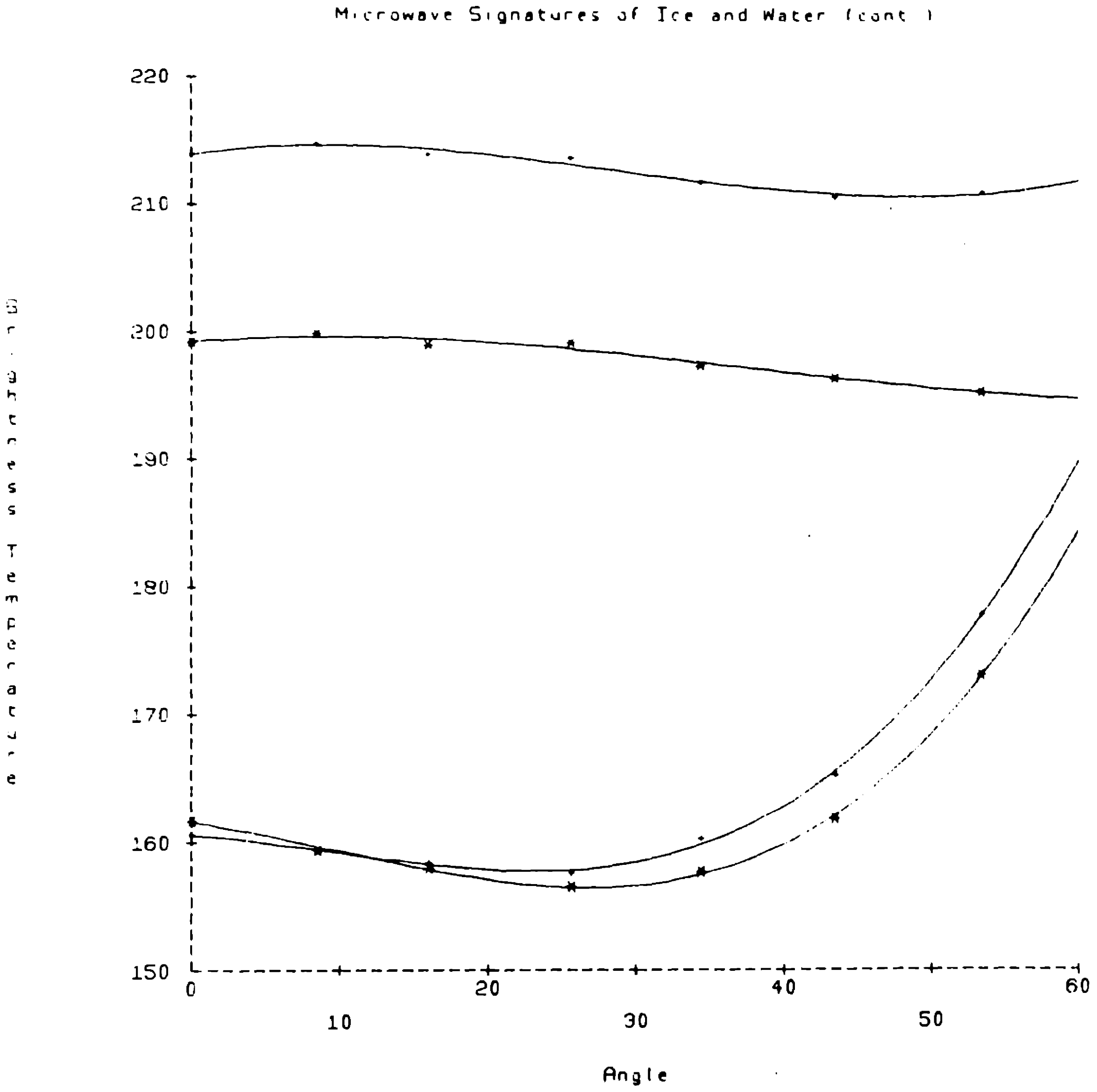

Figure 6 (Cont.): More microwave signatures of ice and water. Curves at ≈ 210° are multi-year sea ice; Curves originating at ≈ 160° are water.

strongly anisotropic and increasing with angle. In contrast the brightness temperature of firn increases as the angle increases. This may indicate a columnar structure for ice and a relatively isotropic one for firn.

A basic research problem[18] that should be solvable using these results is the ability to distinguish between a mixture of new sea ice with water and old sea ice. From nadir data alone this is difficult; since new sea ice is very bright (approximately 240°K) and water is very dark (approximately 160°K), an equal mixture of the two will be approximately 200°K, the same temperature as old sea ice. However, the angular data will differ for the two surfaces. Since water brightens as the angle increases,[19] the brightness temperature of a mixture of new sea ice and water should show an increase with angle while the brightness temperature of multi-year sea ice decreases.

Preliminary studies of the orthogonal vector components using the fourteen-dimensional axis rotating program indicate that each fourteen member vector has at most six or seven important components. An initial clustering process on the first seven orthogonal components was attempted. The resulting map (Map 9) is very similar to the clustering map which uses the primary data, indicating that little important information was

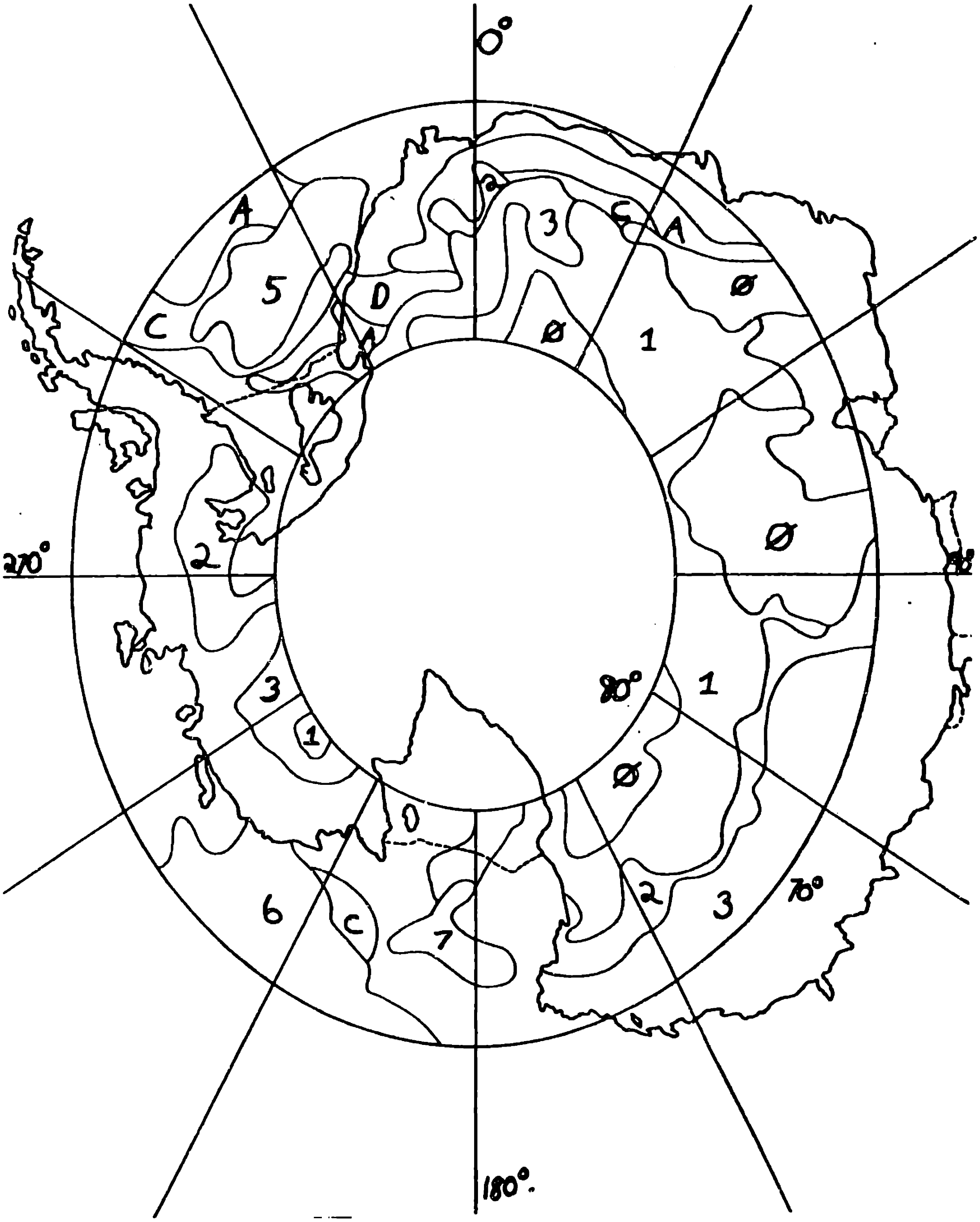

Map 9: Clustered map of Antarctica based on seven orthogonal components of the original September dataset. Symbols for the different clusters are arbitrary.

lost in reducing the fourteen dimensional space to seven dimensions. I suggest that additional runs be made to observe the significance of each orthogonal component and the physical parameters to which they correspond.

A K-nearest neighbors program was used which tests experimental vectors and assigns them to classes based on their K closest pre-defined vectors. Using data from January as the ten defined classes, each with ten vectors, the datasets from November, September, and January were tested. Maps 10, 11, and 12 show the results. Migration of the contour lines towards the poles during the summer can be observed, presumably following seasonal temperature variations. Note how cluster 9 expands to fill Eastern Antarctica in the winter and follows the decrease in surface temperature. Cluster 8 represents the extent of sea ice. Future work will include the selection of a set of theoretical vectors to better identify experimental data.

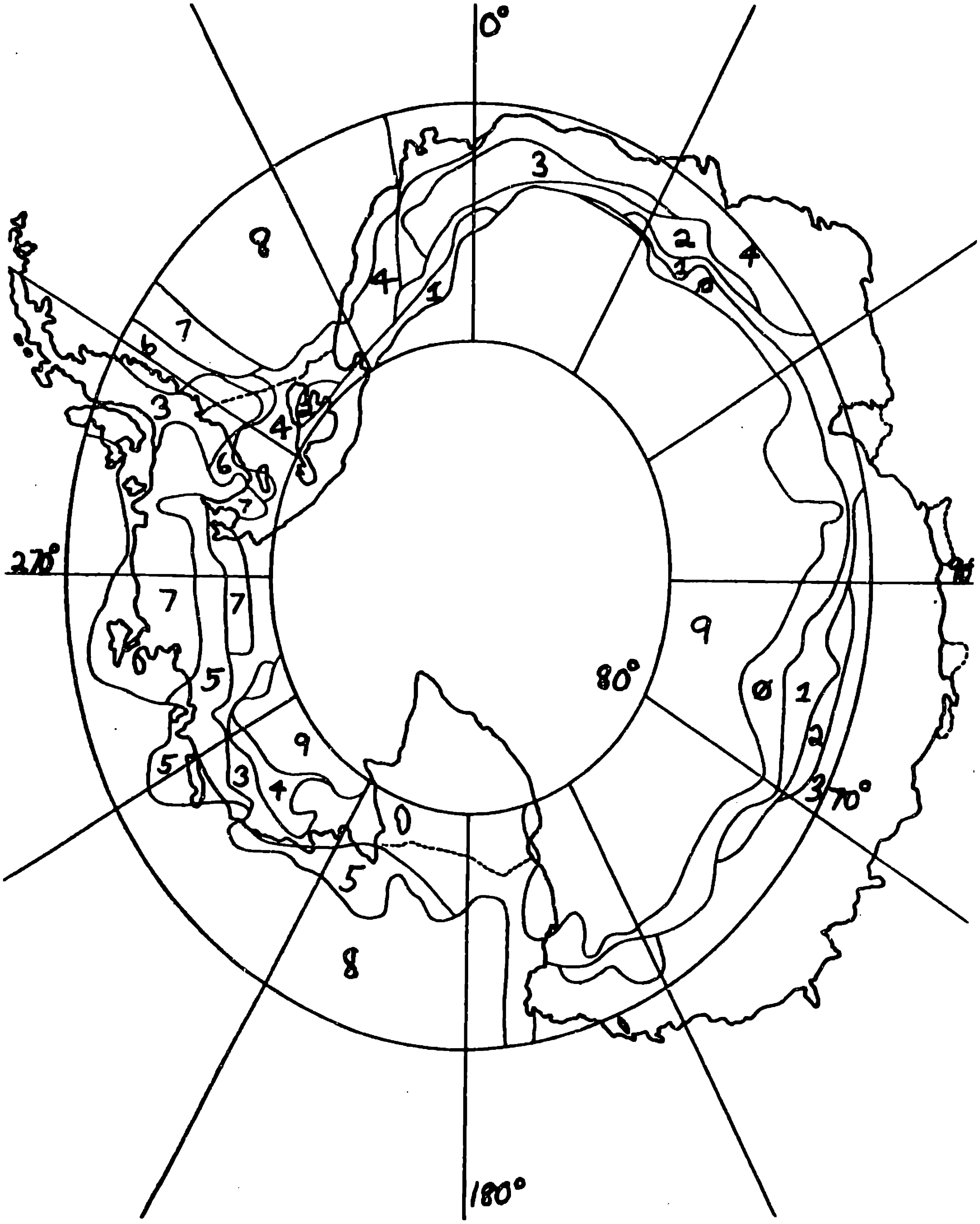

Map 10: K-nearest neighbors map using ten classes defined from January data on the September dataset. Symbols for the different clusters are arbitrary.

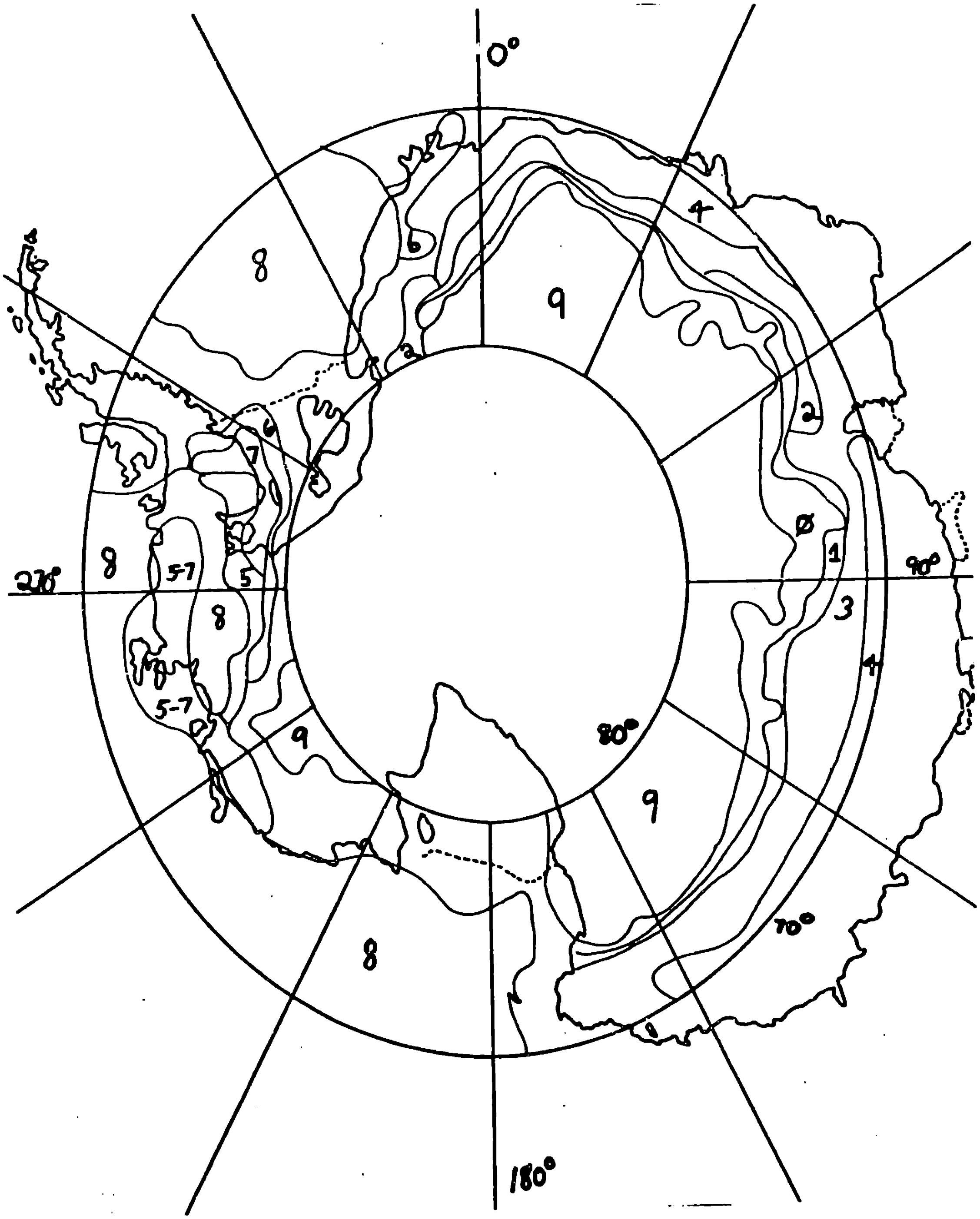

Map 11: K-nearest neighbors map of Antarctica using 10 classes defined from January data on the November dataset. Symbols for the clusters are arbitrary. (The "5-7" cluster represents a mixture of the "5" and the "7" cluster).

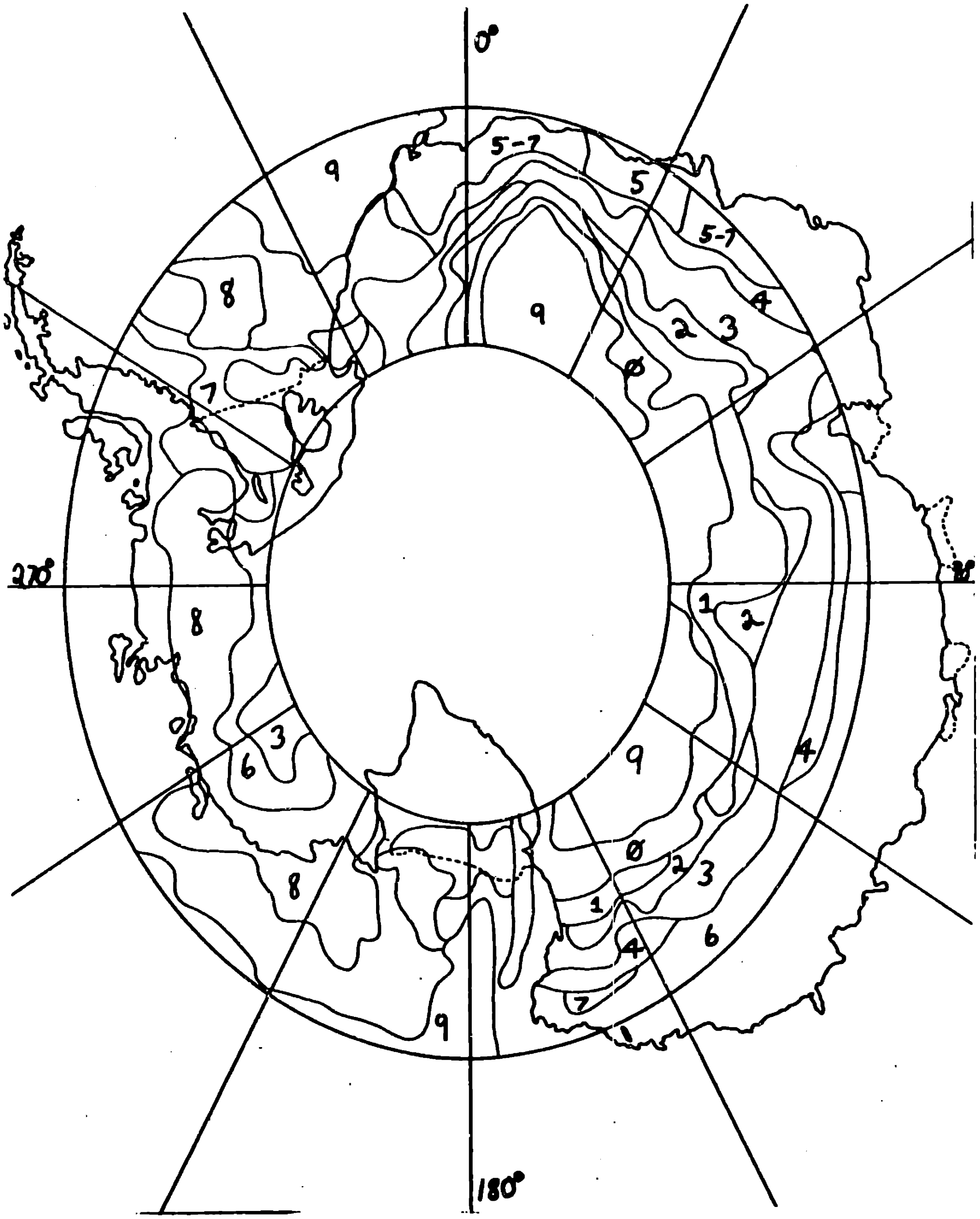

Map 12: K-nearest neighbors map of Antarctica using ten classes defined from January data on the January dataset.

CHAPTER 5 -- THEORY OF SNOW SCATTERING

In this chapter, I shall analyze the observed brightness temperature of snow using two parameters: the scattering and absorption constants of the snow medium. Assuming an absorption coefficient and a temperature profile which are constant with depth in the firn and a linear relation between the scattering coefficient and the depth, a closed form solution to the equation of radiative transform yields equation 5-8. A relation between the accumulation rate and the scattering parameter is then calculated; equation 5-29, which relates the microwave emissivity to the accumulation and the ten meter temperature, enables the conversion of observed brightness temperature to predictions of accumulation rates.

The radiation measured by a satellite observing the earth's surface has three components: (1) the radiation emitted from the ground and attenuated by the atmosphere, (2) the downwelling radiation of the atmosphere which is reflected by the snow and then attenuated by the atmosphere, and (3) the upwelling radiation of the atmosphere. Kunzi et al.[1] have shown that the effects of the latter two components of radiation and the attenuation of the atmosphere can be ignored for the Antarctic and Greenland regions. Thus, the brightness temperature observed by the Nimbus-6 satellite is approximately the brightness temperature of the snow due to its internal radiation flux.

The brightness temperature depends on both the absorption and scattering coefficients of the snow. The equation of radiative transfer in the medium can be approximated in the case of a small scattering to absorption ratio as:[3]

$$T_b = \int_0 T(z)e(z)g(z)dz \qquad (5\text{-}1)$$

where T_b is the brightness temperature, $T(z)$ is the physical temperature of the snow as a function of depth, and $e(z)$ is the emittance or albedo of the snow:

$$e(z) = \frac{K_a(z,T)}{K_e(z,T)} \qquad (5\text{-}2)$$

$$= \frac{K_a(z,T)}{K_a(z,T)+K_s(z,T)}$$

Here K_a (z,T), K_s (z,T) and K_e (z,T), which are the absorption, scattering, and extinction coefficients respectively, are functions of depth and temperature. $g(z)$ is the radiative transfer function which, for small scattering, can be approximated as:

$$g(z) = K_a(z,T)\exp[-\tau(z)] \qquad (5\text{-}3)$$

where

$$\tau(z) = \int_0^\infty K_e(z,T)\,dz \qquad (5\text{-}4)$$

Thus equation 5-1 now becomes

$$T_b = \int_0^\infty K_a(z,T) \exp\left[-\int_0^z K_e(z,T)\,dz\right] dz \qquad (5\text{-}5)$$

I will now analyze equation 5-5 using Zwally's assumptions[3] that the scattering and absorption coefficients of snow can be modeled as

$$K_s(z,T) = Kz \qquad (5\text{-}6)$$

and

$$K_a(z,T) = K_a(T) \qquad (5\text{-}6A)$$

The viability of this physical model of the snow will be discussed later in this chapter.

Two specific cases can be readily analyzed: (1) $T(z) = T_{10}$ and (2) $T(z) = T_1 \exp(-fz)$. For Case 1, equations 5-5, 5-6, and 5-6A result in

$$\begin{aligned} T_b &= T_{10} \int_0^\infty K_a(T) \exp\left\{-\int_0^z \left[K_a(T) + Kz\right] dz\right\} dz \qquad (5\text{-}7) \\ &= T_{10} \int_0^\infty K_a(T) \exp\left\{-\frac{1}{2} K \left[z + \frac{K_a(T)}{K}\right]^2\right\} \\ &\quad \cdot \exp\left[\frac{K_a^2(T)}{2K}\right] dz \end{aligned}$$

Here K_a and K are properties of the medium for a specific frequency. Let

$$X = \frac{K_a(T)}{\sqrt{2K}} \qquad \text{and} \qquad v = \sqrt{\frac{K}{2}}\left[z + \frac{K_a(T)}{K}\right]$$

We now have

$$T_b = 2 T_{10}\, x \exp(x^2) \int_x^{\infty} \exp(-v^2)\, dv \tag{5-8}$$

Let

$$Z(x) = \frac{T_b}{T_{10}} = \sqrt{\pi}(x)\left[\exp(x^2)\right]\left[1 - \phi(x)\right] \tag{5-8A}$$

where $\phi(x)$ is the standard error function. Note that Z(x) equals the emissivity E of the medium when the temperature profile is a constant. The emissivity is displayed as a function of x in Figure 7 for this case.

A rational expression for Z(x) will now be derived. A very good approximation for the error function $\phi(x)$ is[20]

$$\phi(x) = \exp(-x^2)\left[1 - (a_1 r + a_2 r^2 + a_3 r^3)\right] \tag{5-9}$$

where

$$r = (1+px)^{-1} \tag{5-10}$$

and p = .47047, a_1 = .34802, a_2 = −.09587, and a_3 = .74857.

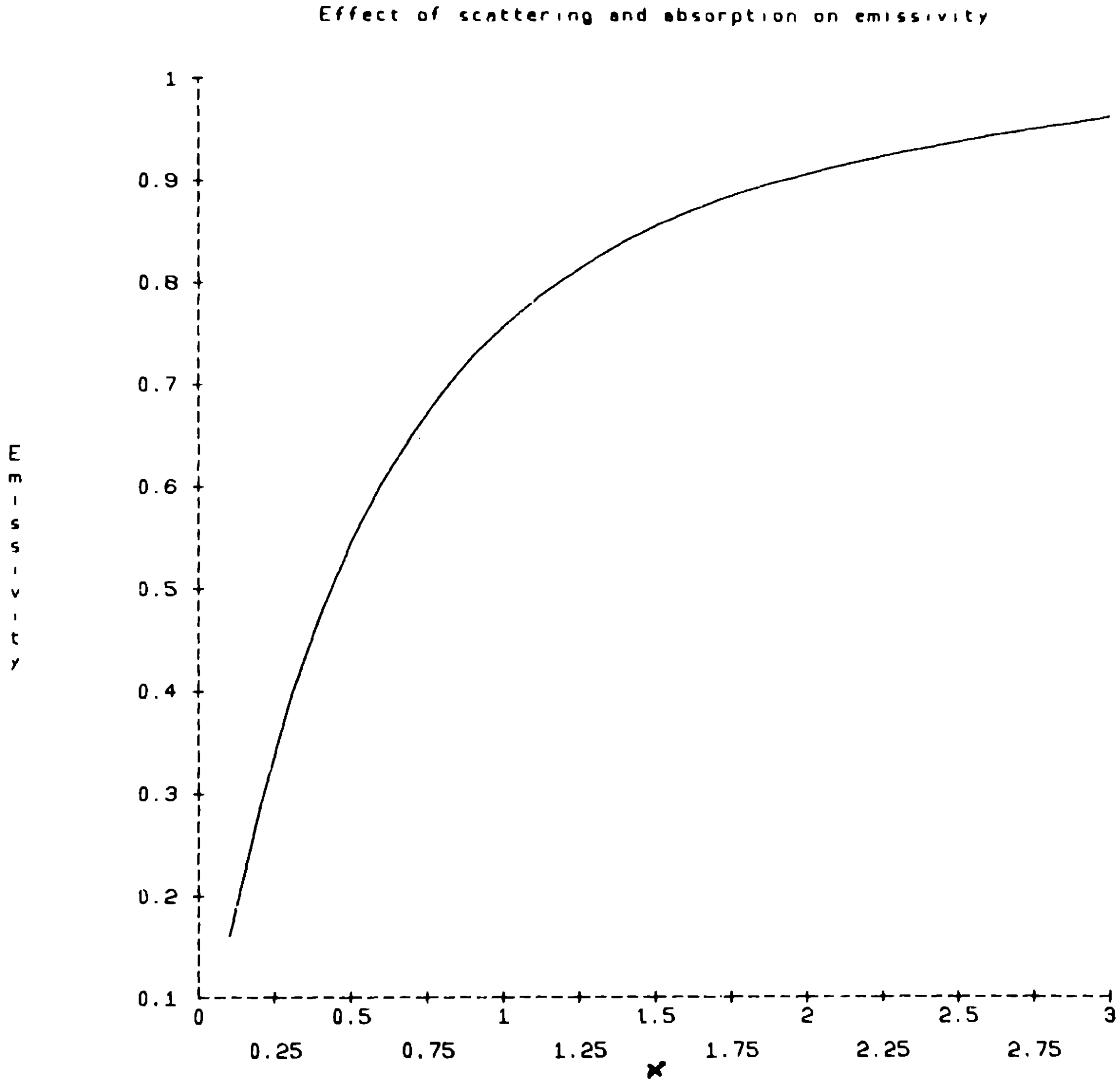

Figure 7: The Z function (representing the emissivity in the constant thermal gradient case) plotted against x (where $x = K_a/\sqrt{2K}$).

The Z function now becomes

$$Z(x) = \sqrt{\pi}\, x\,(a_1 r + a_2 r^2 + a_3 r^3) \qquad (5\text{-}11)$$

For the second case, $T(z) = T_1 \exp(-fz)$, the brightness temperature is computed as

$$T_b = \frac{T_1 K_a(T)}{K_a(T)+f} \int_0^\infty [K_a(T)+f] \cdot \exp\left\{-\int_0^z [(K_a[T]+f)+Kz]\, dz\right\} dz \qquad (5\text{-}12)$$

The integrals in equations 5-5 and 5-12 are identical except for the change from $K_a(T)$ to $[K_a(T) + f]$ Therefore, for case 2,

$$T_b = \frac{T_1 K_a(T)}{K_a(T)+f}\, Z\left(\frac{K_a(T)+f}{\sqrt{2K}}\right) \qquad (5\text{-}13)$$

Actually any combination of constant or exponential dependence of temperature and constant or linear dependences of absorption and scattering with firn depth can be solved using some variation of the parameters $K_a(T)$ and K in the function Z. In my analysis, the scattering coefficient varied linearly and the absorption coefficient remained constant with depth;

these choices appear to model the snow properties correctly as the following discussion shows.

The two parameters $K_a(T)$ and K determine the observed emissivity uniquely. The absorption coefficient $K_a(T)$ is computed as[1]

$$K_a(T) = \frac{2\pi \nu \epsilon''}{c(\epsilon')^{1/2}} \qquad (5\text{-}14)$$

where ν is the radiation frequency, c is the speed of light, and ϵ'' and ϵ'' are the imaginary and real parts of the dielectric constant of the snow respectively. ϵ' is independent of frequency and temperature while ϵ'' increases with temperature at a rate of approximately 1.6%/°K and increases slightly with frequency. To facilitate computations, the temperature dependence of ϵ'' is approximated as linear and its frequency dependence is neglected. Both ϵ' and ϵ'' are dependent on snow density, which varies for Antarctica from 0.35 to 0.55 grams cm^{-3}. For this density range, $\epsilon' = 1.8$ and $\epsilon'' = 6.3 \times 10^{-4}$ at 256°K and 3.0×10^{-4} at 213°K. Using these parameters, the absorption coefficient $K_a(T)$ has been calculated from equation 5-15 as a function of ν and T and is presented in Table 1. We have

$$K_a(T) = 15.4\,\nu \left(3.0 \times 10^{-4} + \left[\frac{3.3 \times 10^{-4}}{43}\right][T - 213]\right) \qquad (5\text{-}15)$$

ABSORPTION COEFFICIENTS

T_{10}	ν=31 GHz.	ν=22 GHz.
213	.15	.10
218	.17	.12
223	.18	.13
228	.20	.14
233	.22	.15
238	.24	.17
243	.26	.18
248	.28	.20
253	.30	.21

Table 1: Absorption coefficients K_a as a function of ground temperature (nepers/meter).

where ν is measured in GHz. Our assumption of a constant coefficient $K_a(T)$ in equations 5-12 and 5-5 implies a constant density of snow as a function of depth and a reasonably constant temperature profile. Since $K_a(T)$ varies only with the most extreme temperatures found in Greenland and Antarctica by a factor of 2, and more detailed information on the temperature gradient is unavailable, this approximation appears both necessary and reasonable.

Calculation of the theoretical scattering coefficient is more difficult since the exact model to be used is not immediately apparent. Chang et al.[2] and Zwally[3] used a spherical model for the snow crystals while Fisher[5] modeled the snow crystals by introducing three-dimensional fluctuations in the refractive index. Second, Zwally[3] found it necessary to multiply the theoretical scattering parameter of the spherical model by 0.12 to obtain agreement with observed emissivities. Third, it is difficult to find all the groundtruth needed to generate the theoretical emissivities and scattering parameters for any assumed model.

Since the scattering coefficient cannot be obtained from available groundtruth data, a semi-empirical approach will be taken. We will assume, a priori, that the scattering coefficient is a linear function of depth; that is $K_s(z) = Kz$. (The physical validity of this assumption is discussed later in this chapter.) We will then solve for K at each observed area from equation 5-8, the ten meter temperature (and hence the dry snow absorption coefficient), and the observed radiometric emissivities.

The relation between the scattering parameter and the accumulation rate must now be considered. An understanding of how snow crystals grow is essential for our analysis. For Antarctic temperatures (217°K to 250°K), the crystals are larger for warmer temperatures and for lower accumulation rates when the snow density is constant. Gow[21] reports that a crystal radius r grows at a rate

$$r^2 = r_o^2 + K_1 \exp(-K_2/T)t \qquad (5\text{-}16)$$

where r_o is the initial radius, T the temperature, t the amount of time the crystal has been growing, and K_1 and K_2 are positive constants (as yet undetermined.) Moreover, the time that a crystal is on the ground and its depth are related by

$$t = \frac{\rho z}{A} \qquad (5\text{-}17)$$

where ρ is the snow density and A is the accumulation rate (both assumed constant). However

$$r^3 = r_o^3 + az \qquad (5\text{-}18)$$

fits the crystal size data for the top ten meters of snow better than equation (5-19); a is a constant determined by the snow in each location. Assuming that $r_o = 0$, equations 5-17 and 5-18 give

$$r^3 = \frac{aAt}{\rho_o} \qquad (5\text{-}19)$$

Equations 5-16 and 5-19 are reconciled by making the approximation that, for the first ten meters of snow, r^2 should be replaced by r^3 in equation 5-16 to give

$$\begin{aligned} r^3 &= K_3 \exp(-K_4/T)\, t \qquad (5\text{-}20) \\ &= K_3 \exp(-K_4/T)\left(\frac{\rho_o z}{A}\right) \end{aligned}$$

The approximation that $r_o = 0$ is weak since, for the first few meters of snow cover, the size of the crystal is influenced by the initial starting size as well as the rate of growth.[21] However, the scattering effect due to this initial crystal size will be incorporated into the empirical coefficients K_{10} and K_{11} of equation 5-29; the scattering effect which is caused by both the initial particle size and the increasing crystal size will be attributed entirely to the latter effect.

If we use the spherical crystal approximation, Gow's data[21] indicates that we are dealing with Rayleigh scattering which is proportional to r^6 for an individual crystal. Since the number of scatterers in a packed volume is proportional to r^3, $K_s(z)$ is proportional to r^3 which implies that

$$k_s(z) = K_5 \exp(-K_4/T) \frac{z}{A} \qquad (5\text{-}21)$$

We now see why our choice of a linear relationship between the scattering and the depth have physical meaning. Since $K_s(z) = Kz$, we have

$$K = K_6 \exp(-K_4/T)/A \qquad (5\text{-}22)$$

Equation 5-8 related the emissivity to the scattering coefficient of the snow. With equation 5-22, I have likewise correlated the scattering coefficient to the accumulation rate. By combining these equations together, my goal of inverting for accumulation rate from microwave emissivities will be achieved.

From equation 5-22, we see that

$$\frac{4}{\sqrt{2K}} = K_7 \exp(K_8/T)\sqrt{A} \qquad (5\text{-}23)$$

Multiplying equation 5-23 by the absorption coefficient, we get

$$\frac{K_a(T)}{\sqrt{2K}} = K_a(T)\, K_7 \exp(K_8/T)\sqrt{A} \qquad (5\text{-}24)$$

$K_a(T)$ can be expressed from equation 5-15 as

$$K_a(T) = K_e\left[1 + .0256(T - 213)\right] \qquad (5\text{-}25)$$

where K_a is a frequency-dependent variable. Defining

$$C(T) = \left[1 + .0256\ (T - 213)\right] \qquad (5\text{-}26)$$

then

$$\frac{K_a(T)}{\sqrt{2K}} = C(T)\ K_9\ evp\left(K_8/T\right)\sqrt{A} \qquad (5\text{-}27)$$

Taking the $Z(x)$ function of each side of equation 5-27 and using equation 5-8 we find

$$Z\left[C(T)\ K_9 \exp\left(K_8/T\right)\sqrt{A}\right] = Z\left[\frac{K_a(T)}{\sqrt{2K}}\right] \qquad (5\text{-}28)$$

$$= E$$

where E is the emissivity (equation 5-8) for the constant temperature profile case. Defining an inverse function to equation 5-8 such that $Z^{-1}[E] = X$ equation 5-28 becomes

$$\left[Z^{-1}(E)\right]^2 = X^2 \qquad (5\text{-}29)$$

$$= C^2(T)\ K_{10} \exp\left(K_{11}/T\right) A$$

Equation 5-29 is the desired expression which gives the non-linear relationship between the emissivity, the temperature and the accumulation. Groundtruth data will be used to determine the parameters K_{10} and K_{11}.

Several problems arise, however, with this model when Rayleigh scattering is assumed. First, the scattering parameter K, as determined from ground-based data, is overestimated and requires an empirical correction factor of 0.12.[3] Second, the observed frequency dependence of the emissivity does not agree with the Rayleigh scattering model, for which crystal sizes are much less than a wavelength. In the constant temperature profile case, the emissivity observed by the 31 GHz. radiometer is given by Equation 5-8 as

$$E_{31} = Z\left[\frac{K_{a31}(T)}{\sqrt{2}\,K_{31}}\right] \tag{5-30}$$

where the subscripts refer to the radiometric frequencies. Since K_a is proportional to frequency and K to frequency to the fourth power in the Rayleigh approximations, the observed 22 Ghz. emissivity should be related to the 31 Ghz. emissivity by

$$E_{22} = Z\left(\frac{K_{a31}}{\sqrt{2}K_{31}}\cdot\frac{\nu_{31}}{\nu_{22}}\right) = Z\left(\frac{K_{a31}}{\sqrt{2}K_{31}}\cdot\frac{31}{22}\right) \tag{5-31}$$

However, observations contradict this conclusion. Table 2 shows ten random points from Antarctica. Note that the actual brightness temperature at 22 GHz. is approximately equal to that at 31 GHz. The same results are obtained from the Greenland data.

Two explanations of this observed frequency dependency seem feasible. First, the major scattering effects may be caused by nearly resonant-sized particles. If the particle dimensions were on the order of a wavelength, one would expect a scattering coefficient proportional to ν^2 rather than ν^4. For a frequency squared relation of the scattering coefficient (without considering any other effects) the brightness temperature at 31 GHz. equals that at 22 GHz. since

$$Z\left(\frac{K_{a31}}{\sqrt{2}K_{31}}\right) = Z\left(\frac{K_{a22}}{\sqrt{2}K_{22}}\right) \qquad (5\text{-}32)$$

Likewise, for scattering caused by three-dimensional fluctuations of the dielectric constant for which the correlation lengths in the media are on the order of a wavelength,[5] the scattering coefficient again depends on ν^2 and yields approximately constant brightness temperatures at 22 and 31 GHz. Analysis of the variation of brightness temperature with angle should assist in determining the correct model for scattering.

COMPARISON OF 31 GHz and 22 GHz DATA

T_{10}	T_{b31}	T_{b22}--PREDICTED	T_{b22}--ACTUAL
248	214	229	215
238	197	213	197
233	183	201	184
232	173	193	174
231	171	191	171
231	171	193	173
230	177	196	176
230	173	193	170
256	207	226	204
251	209	226	209
246	181	203	180
240	172	194	170
236	170	191	169

Table 2: Shown here for several typical points in Antarctica are T_{10} (the ten-meter temperature), T_{b31} (the 31 GHz. brightness temperature), T_{b22}--PREDICTED (the 22 GHz. brightness temperature as predicted from T_{b31} by a scattering proportional to ν^4), and T_{b22}--ACTUAL (the 22 Ghz. brightness temperature actually observed.) The T_{b22}--PREDICTED is on average 20° higher than the actually observed brightness temperature.

Our analysis thus indicates that the simple single particle Rayleigh scattering which led to the proportionality between K and r^3 does not correspond to the satellite observations of brightness temperature. However, we will continue to assume a proportionality between K and r^3 for two pragmatic reasons: (1) The correlation distance for the dielectric fluctuations in the media (or the resonant-sized snow crystals) and, hence, the scattering coefficient K would reasonably be expected to increase with both time and temperature at approximately the same rate as the individual crystals. (2) The assumption that K is proportional to r^3, which leads to Equation 5-29 gives remarkably good predictions of snow accumulation as shown by both Zwally[3] and the present analysis. However, additional theoretical studies are required to explain these observations.

CHAPTER 6 -- EXPERIMENTAL RESULTS FOR SNOW ACCUMULATION

Snow accumulation maps, based on the satellite radiometric data, will now be derived. The basic relation between snow accumulation A, temperature T, and emissivity E is:

$$\frac{[z^{-1}(E)]^2}{[C(T)]^2} = K_{10}\exp(K_{11}/T)\,A \qquad (5\text{-}29)$$

A dataset of approximately 300 geographical points spread uniformly over Antarctica for November 1975 was used for which values of ten meter temperature $T_{10} = T$ and snow accumulation rate A were known.[10,11] The data were separated into two independent groups, each of eight sub-groups within which the physical temperature is constant (to within five degrees). Linear regression analysis was used to calculate the values of $K_{10}\exp(K_{11}/T)$ from equation 5-29, observed values of emissivity at 31 GHz. and snow accumulation for each temperature range (plots of $[z^{-1}(E)]^2/[C(T)]^2$ versus A where $z^{-1}(E)$ and C(T) are obtained from equations 5-29 and 5-26 respectively.) A second least squares run was then performed on the values of $K_{10}\exp(K_{11}/T)$ which were found at the different temperatures for each sub-group, to calculate K_{10} and K_{11}. The data for this run is given in Table 3; the fit for K_{10} and K_{11} are shown in Figure 8. The best values for K_{10} and K_{11} obtained by this analysis were $K_{10} = 6\text{x}10^{-12}$

LEAST SQUARES FIT DATA FOR K_{10} AND K_{11}

T_{10}	$1/T_{10}\times10^3$	Y
253	3.95	-5.07
248	4.03	-4.51
248	4.03	-4.50
243	4.11	-3.80
243	4.11	-3.77
238	4.20	-3.73
233	4.30	-3.08
228	4.38	-3.09
228	4.38	-3.30
223	4.48	-1.85
223	4.48	-2.14
218	4.59	-1.39
218	4.59	-1.39

Table 3: Data for least squares analysis to solve for K_{10} and K_{11}. Basic equation is $y=\ln(K_{10})+K_{11}x$ where $x=1/T_{10}$ and $y=\ln\left(\frac{[z^{-4}(\text{[illegible]})^{2}]}{[C(T)]}\right)$ for different values of T_{10}. (Only thirteen points are used here out of a maximum sixteen. The other three were not available.)

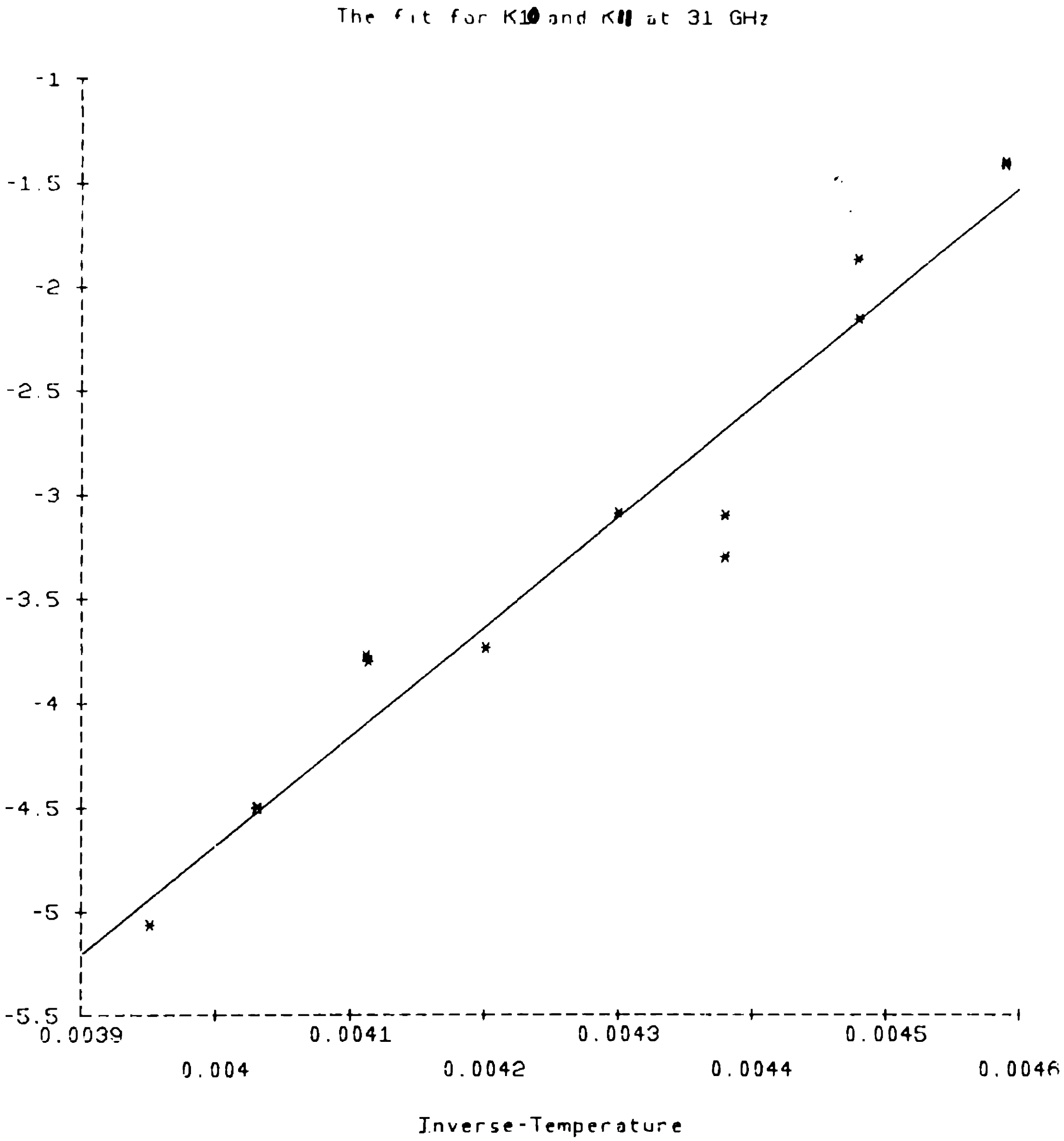

Figure 8: The closest fit for the data in Table 3. The best fit was $K_{10} = 6 \times 10^{-12}$ and $K_{11} = 5288$.

and $K_{11} = 5288$. Using these values, equation 5-29 for 31 GHz. becomes

$$[z^{-1}(E)]^{2} = 6\times10^{-12}[C(T)]^{2}\exp\left(\frac{5288}{T}\right) A \qquad (6\text{-}1)$$

Maps of Antarctic snow accumulation were made from equation 6-1 and the observed microwave emissivity and physical temperature data as a function of latitude and longitude. Maps 13 and 14 compare the geographic contours of snow accumulation in Antarctica measured by ground data with that predicted from 31 GHz. data.

Interesting similarities and disagreements between the radiometric and the groundtruth data are noted. First, both the banded structure of the accumulation rate trends in Eastern Antarctica (between 0° and 150°E) and the two patches of extremely low accumulation rate in the 77°-79°S, 120°E and 77°-79°S, 30°E regions are similar in the two maps. The very high accumulation areas of Western Antarctica and the area of relatively low accumulation at 77°-79°S, 120°-150°W are likewise observed in both maps. This latter region is significant, since a low temperature area of roughly the same shape occurs at approximately 77°-79°S, 100°W. If we had erroneously been observing the effects of the temperature contours instead of

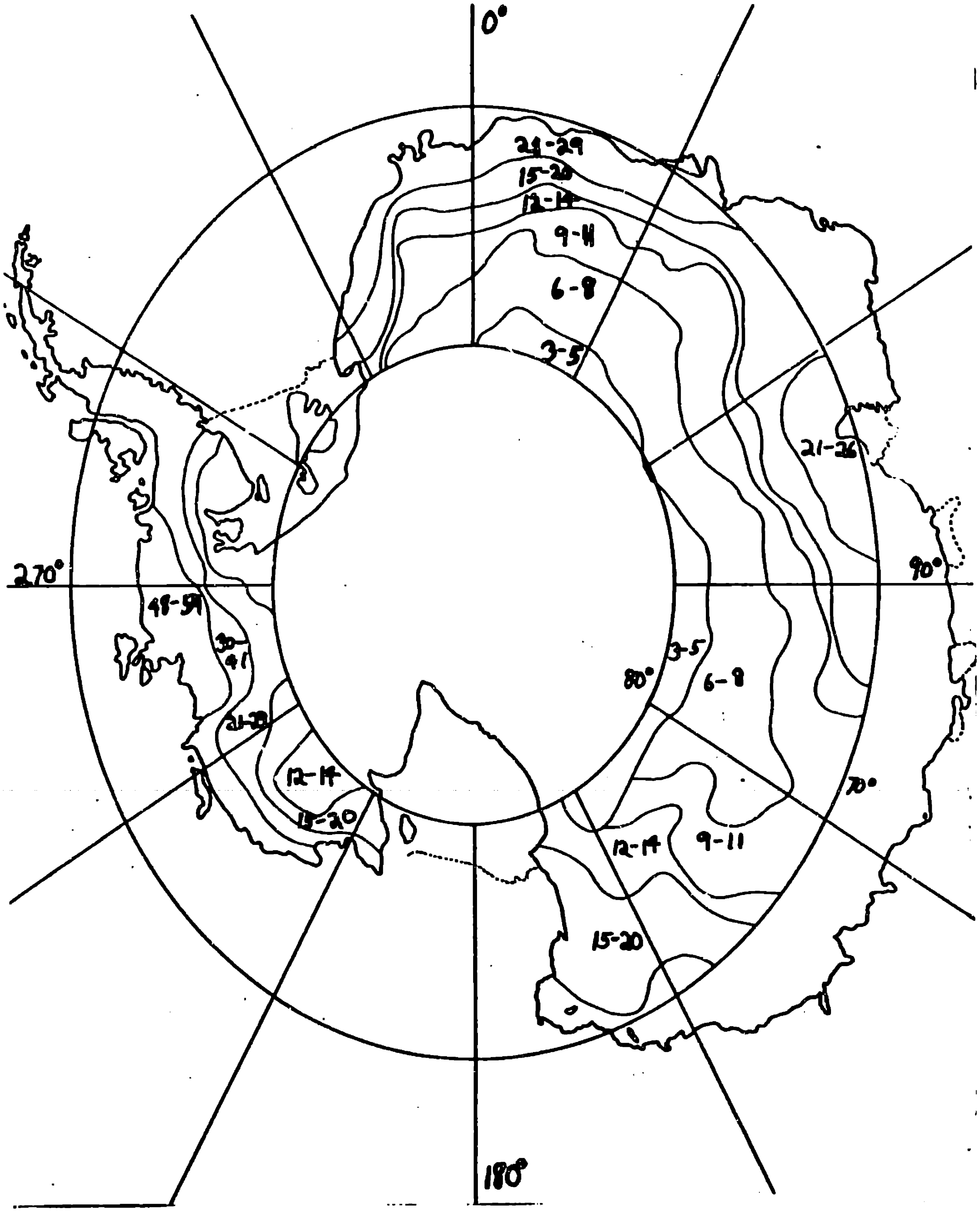

Map 13: Groundtruth accumulation rate map for Antarctica. Note the ellipitical projection used in this map (compared to Map 3). Accumulation rates are measured in gm/cm^2-year.

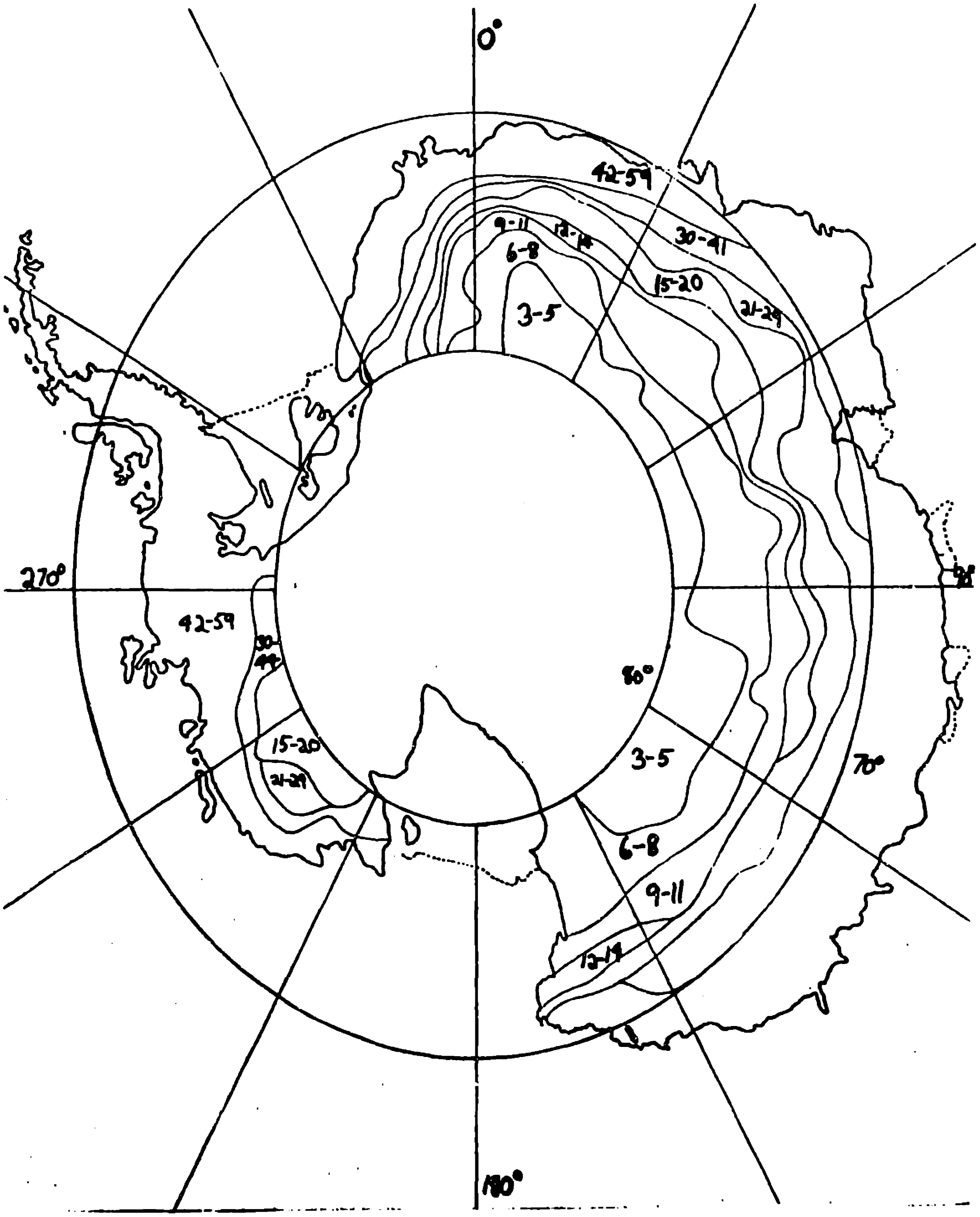

Map 14: Accumulation rates in Antarctica based on 31 GHz emissivities. Contours often follow those in Map 13. Accumulation rates are given in units of gm/cm^2-year.

accumulation trends, the gradients on accumulation maps would have been shifted to the east.

Some of the differences in the two maps seem to favor the emissivity data over the ground observations for predicting snow accumulation. The groundtruth accumulation map (by the American Geographical Society)[10] indicates a wedge shape contour of approximately 18 gm/cm^2-yr. in the 70°-75°S,150°W region that does not follow the band patterns. Our data indicates, instead, that the band pattern continues through this region.

The Greenland analysis was even more successful than that for Antarctica, as can be seen by comparing Map 15 (groundtruth data) with Map 16 (radiometric data). This agreement is particularly significant since the Greenland groundtruth data is probably more accurate[11] than that in the Antarctic. Although the snow accumulation rate contours in the two maps are essentially the same, the 15 gm/cm^2-yr. area in the northern latitudes of Greenland in Map 15 has been resolved into the 9, 12, and 15 gm/cm^2-yr. contours of Map 16. The irregular contour lines in the western part of Greenland at 70°-72°N for the groundtruth data of Map 15 is now smoothed into a wedge-shaped region on Map 16, with accumulation rates ranging from 30 to 40 gm/cm^2-yr. of snow. It

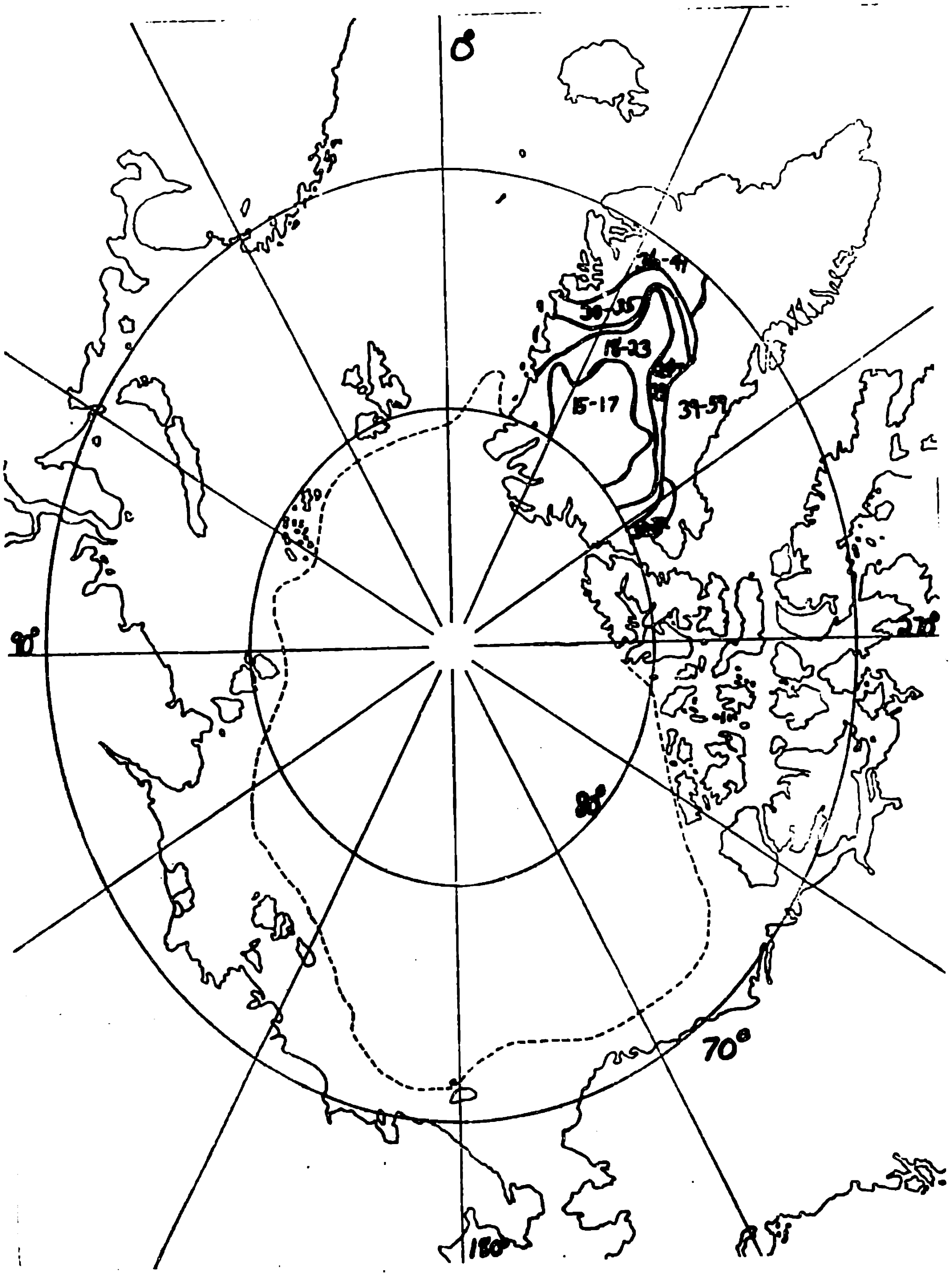

<u>Map 15:</u> Groundtruth accumulation rate map for Greenland. Accumulation rate is measured in gm/cm^2-year. Note that the 15 gm/cm^2-year area is in reality composed of 9, 12, and 15 gm/cm^2-year regions.

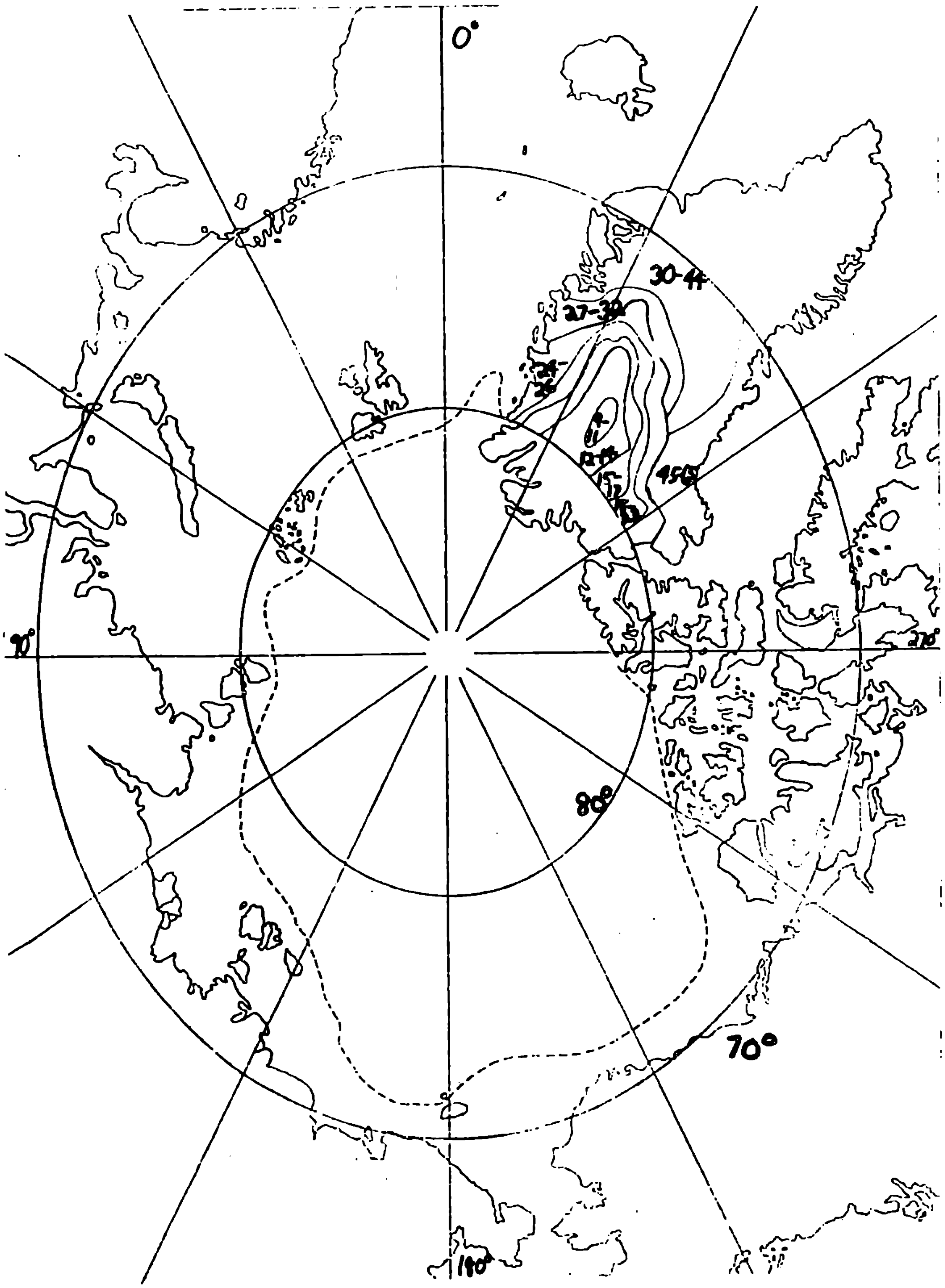

Map 16: Accumulation rate map of Greenland for 31 GHz emissivities. Note how contours approximately follow those of groundtruth accumulation rate map. Accumulation rates are in units of gm/cm^2-year.

must be emphasized that the Greenland data was not used in selecting the coefficients K_{10} and K_{11} (which were derived solely from the Antarctic measurements) and therefore represent an apparently successful and independent test of our procedures.

The identical procedure was followed for the 22 GHz observations. K_{10} and K_{11} were derived by the same regression analysis; the best fit was $K_{10} = 2.55 \times 10^{-10}$ and $K_{11} = 4441$. The results in Antarctica are presented in Map 17.

Since K_{11} changes by a factor of 100, it would seem that we have a serious problem. However, one must first examine the nature of the data in Antarctica. The average ten meter temperature is approximately 228°K; the ten meter temperature rarely goes above 255°K. Thus we can write $K_{10}\exp(K_{11}/T)$ as $K_{10}\exp(K_{11}/(T_0+\Delta T))$ where T_0 is 235°K and ΔT is a small increment (or decrement) in temperature. This leads to the approximation

$$\frac{K_{11}}{T_0+\Delta T} \cong \frac{K_{11}}{T_0}\left(1-\frac{\Delta T}{T_0}\right) \tag{6-2}$$

and

$$K_{10}e^{K_{11}/T} \cong K_{10}\,e^{K_{11}/T_0}\cdot e^{-\frac{K_{11}\Delta T}{T_0^2}} \tag{6-3}$$

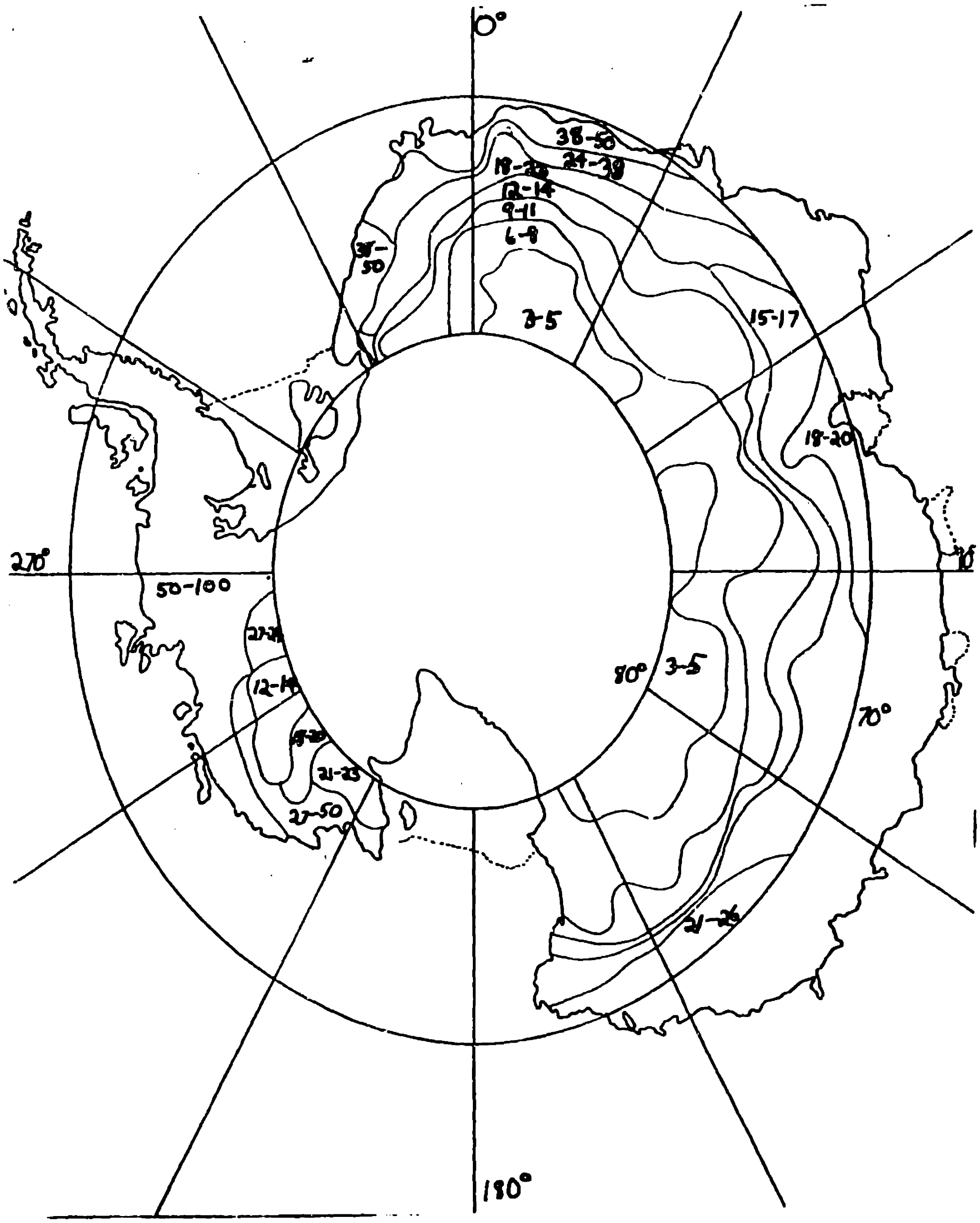

Map 17: Accumulation rate contours based on 22 GHz emissivities. Accumulation rates are measured in gm/cm^2-year.

$K_{10}exp(K_{11}/T_0)$ has almost the same value (approximately .043) for both the 31 and 22 GHz. regression analyses. The important change occurs in the term $exp(-K_{11}\Delta T/T_0^2)$. For positive ΔT, the predicted accumulation increases monotonically with K_{11} for a constant emissivity, while for negative ΔT , it decreases. In general, a larger value of K_{11} provides a larger range of accumulation values for a given range of temperature.

A new map has been generated for Greenland (see Map 18) using the coefficients for 22 GHz. The shapes of the accumulation contours were similar to those found at 31 GHz. However, consistently lower accumulation rates for the area in Central Greenland than predicted by either the 31 GHz or the groundtruth data are found. A possible explanation of this phenomenon is given in the next chapter.

A third accumulation map was generated using a combination of 31 and 22 GHz. brightness temperatures. A joint emissivity was generated of the form $E_r = C_1(T)\ E_{31}+(1-C_1(T))E_{22}$ where E_{31}, E_{22}, and E_r are the 31 GHz, 22GHz, and the linearly combined emissivities respectively and $C_1(T)$ is the weighting factor for 31 GHz. (which is a function of temperature.) Areas of Antarctica and Greenland which were differentiated on the basis of their physical temperature were examined; given the accumulation and the temperature, one can generate a pre-

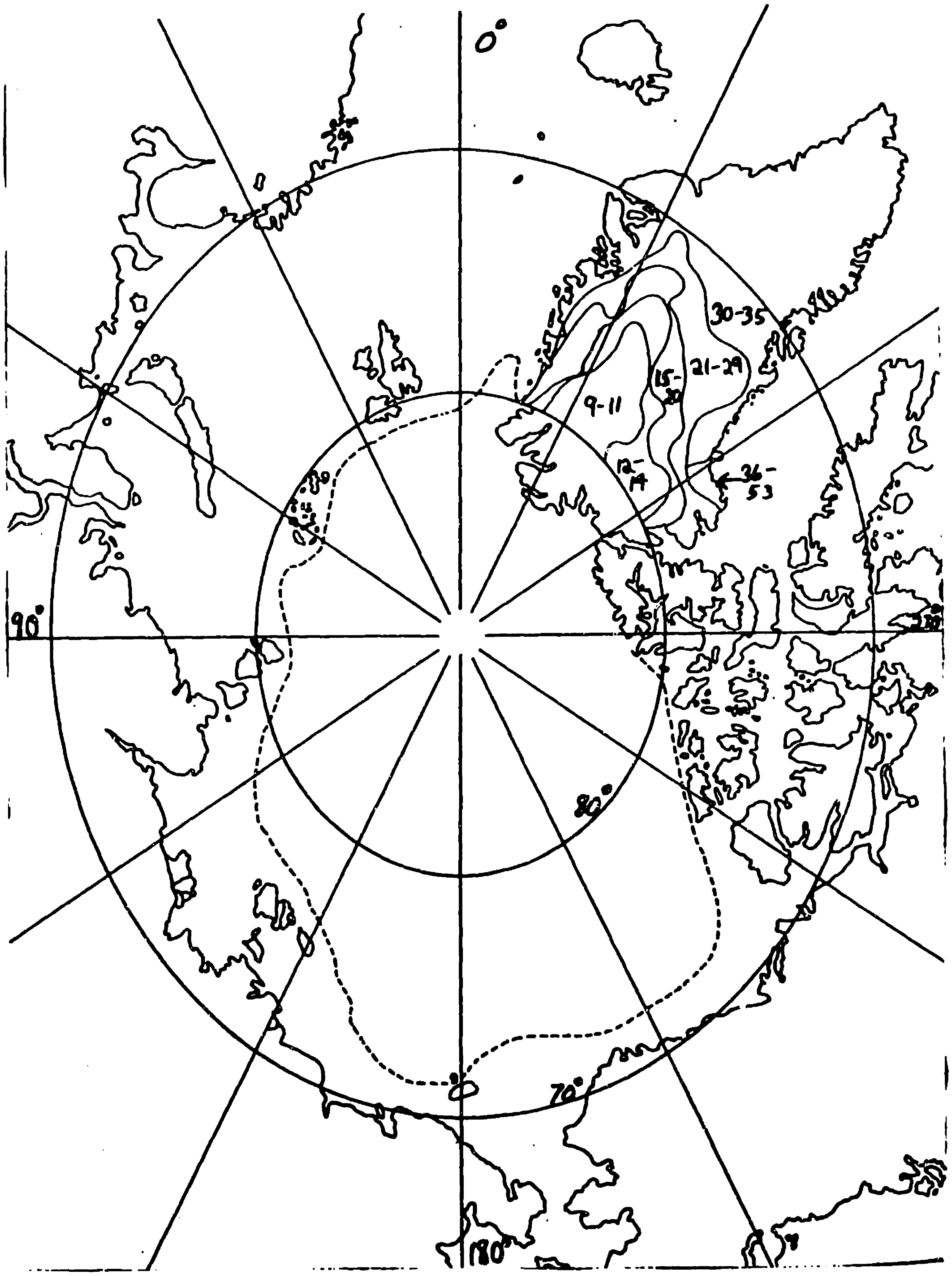

Map 18: Accumulation rate map of Greenland based on 22 GHz emissivities. Predictions are consistently lower than those of groundtruth accumulation map. Accumulation rates are in units of gm/cm^2-year.

dicted emissivity E_p using equation 5-29. A least-squares fit was made to find which value of $C_1(T)$ would cause E_r to best match E_p. It was found that the optimum approximation for $C_1(T)$ is:

$$\begin{aligned} C_1(T) &= 1 && T < 223 \\ C_1(T) &= 1-\frac{(T-223)}{15} && 238 > T \geq 223 \\ C_1(T) &= 0 && T \geq 238 \end{aligned} \qquad (6\text{-}4)$$

Thus low temperatures are best approximated by 31 GHz. data alone and high temperatures by 22 GHz.

The accumulation maps for the joint 22-31 GHz observations are shown for Greenland and Antartica (Maps 19 and 20). The coefficients K_{10} and K_{11} used for this map were $K_1 = 5288$ and $K_2 = 6x10^{-12}$. Since very little difference exists between the 31 GHz. and 22 GHz. brightness temperatures, the basic contours which were generated from these two datasets remain similar. These calculated values of snow accumulation match the measurements made on the ground to a high degree.

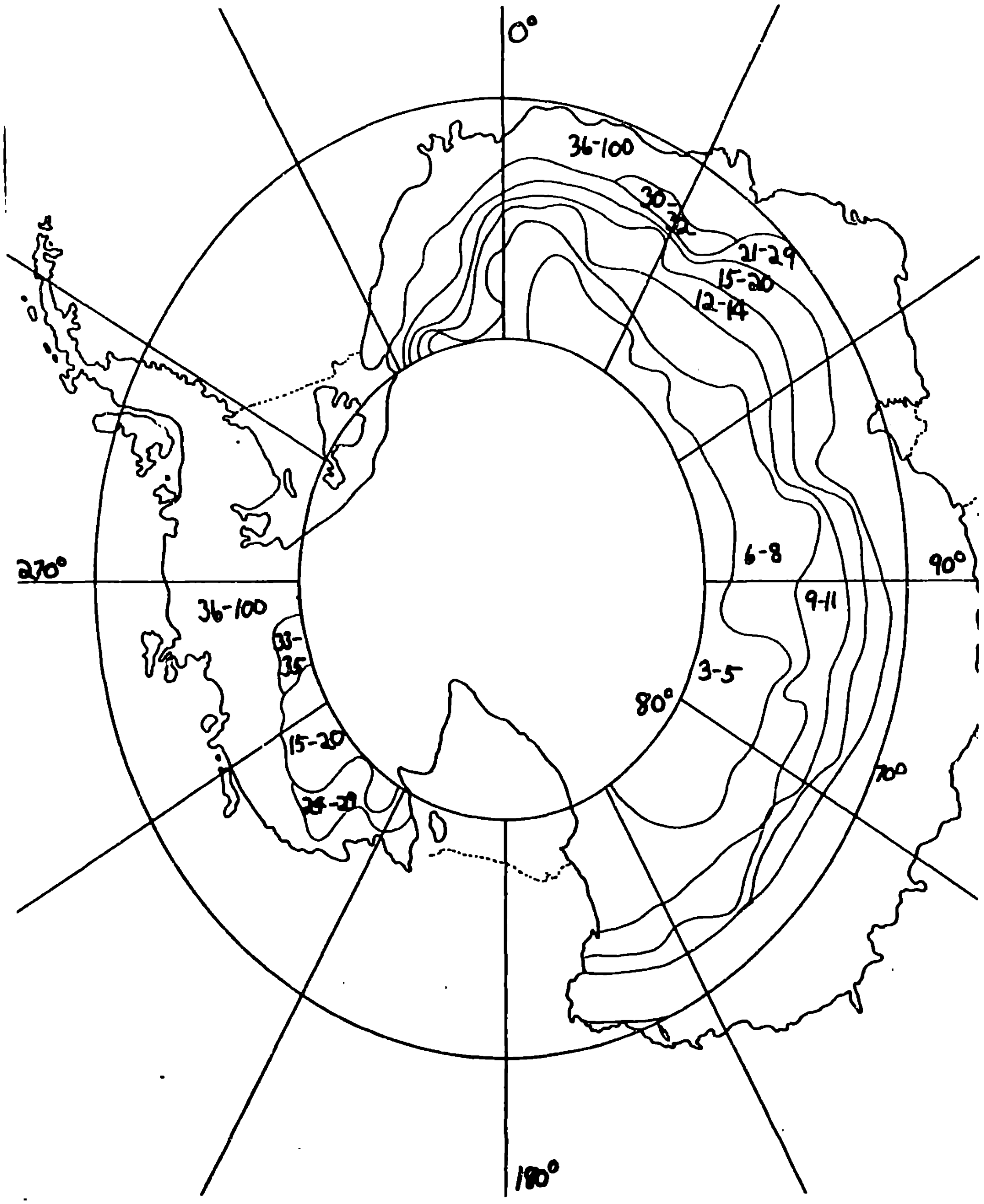

Map 19: Accumulation rate map for Antarctica using composite 31 and 22 GHz emissivities. Accumulation rates are in gm/cm^2-year.

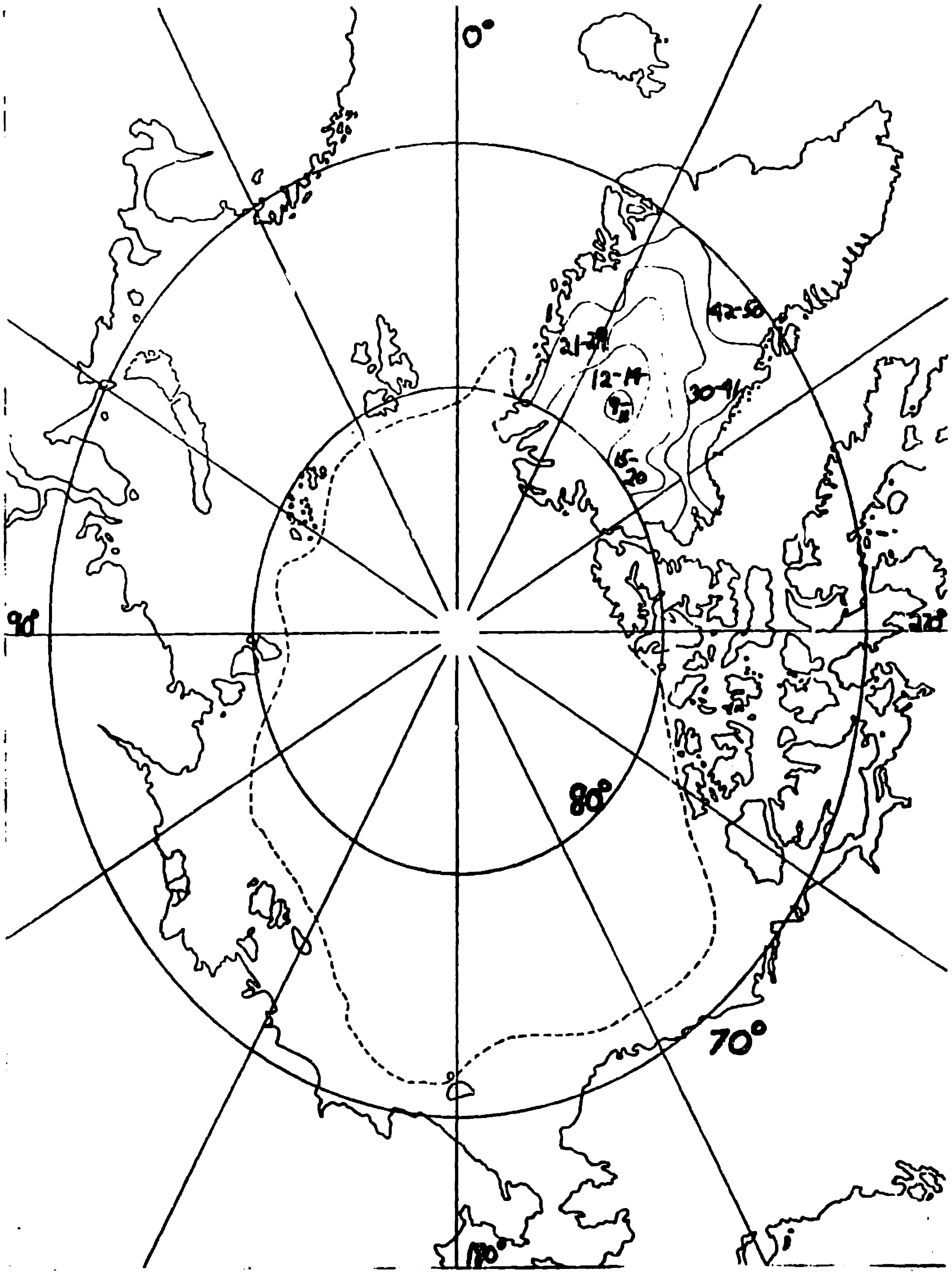

Map 20: Accumulation rate map for Greenland using composite 22 GHz and 31 GHz emissivities. Accumulation rates are measured in gm/cm^2-year.

CHAPTER 7 -- EFFECTS OF THE THERMAL GRADIENT

I have shown previously that the scattering coefficient of the snow likely follows a frequency squared dependence. Furthermore, the relation leads to the same value of brightness temperature for a uniform temperature medium irrespective of frequency. However, the temperature variation with depth of actual snow can account for differences in the brightness temperatures at the two frequencies of observation.

The depth of penetration d_p of microwaves in snow ($d_p \approx \frac{1}{K_s(z,T) + K_a(z,T)}$) tends to decrease with increasing frequency since both scattering and absorption effects increase. For a non-constant temperature profile, the 31 GHz. radiometric measurements are influenced by the snow temperatures nearer the surface more than those at 22 GHz.

Figure 9, derived from equation 2-2, shows that a thermal bulge at approximately two to three meters depth has formed in Antarctica during the November transition from winter to summer. The presence of this bulge was neglected previously where a constant temperature profile was assumed. Figure 10 is a plot of the difference between the brightness temperatures ($\Delta T_{b22-31} = T_{b22} - T_{b31}$) as the scattering increases for

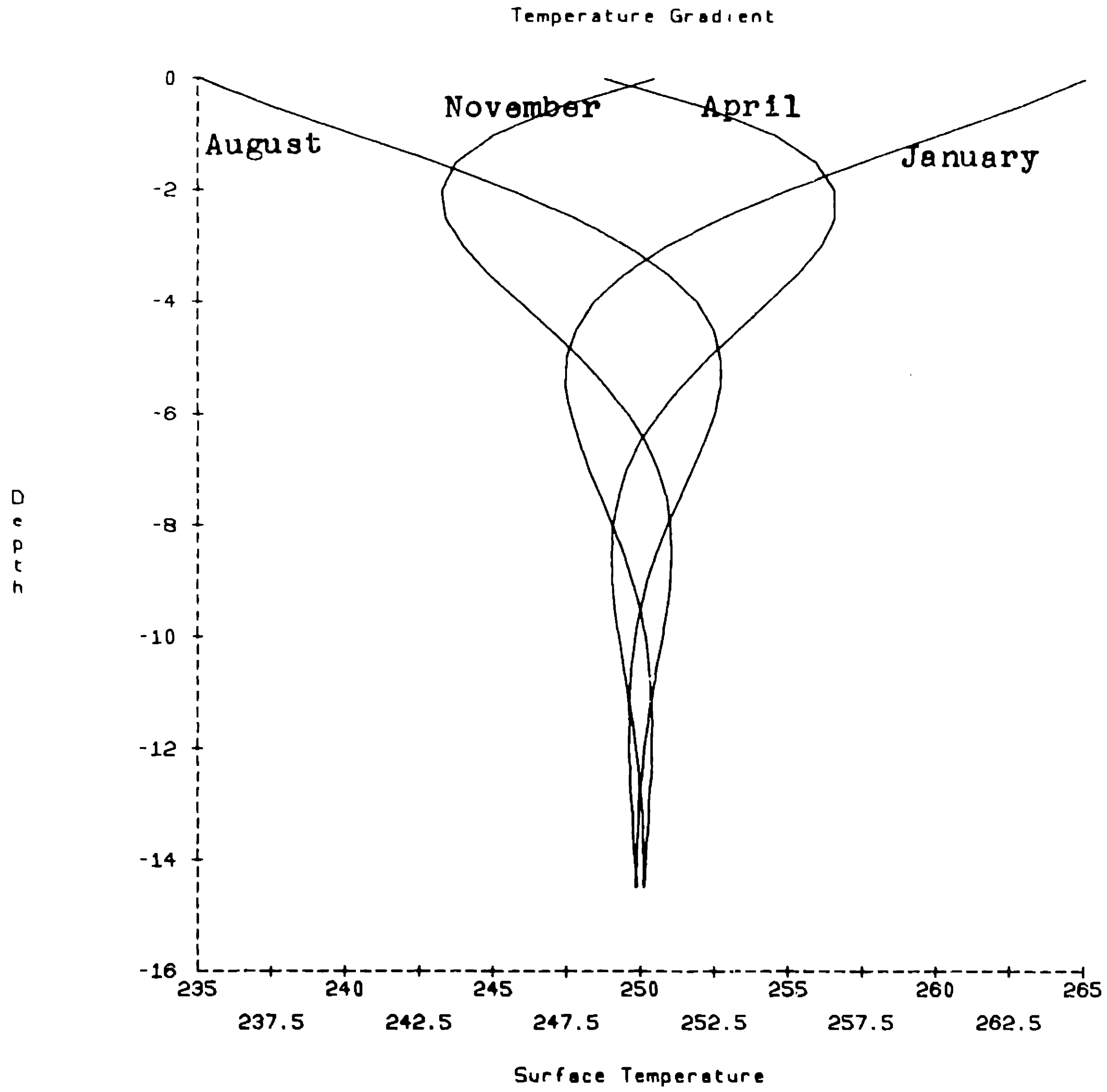

Figure 9: A model temperature gradient for Antarctica.[3] This is derived from equation 2-2 where $T_{10} = 250$, $f = .3$, $a_1 = .5$, $a_2 = 1$, and $a_3 = 0$. Note the non-exponential gradients in November and April.

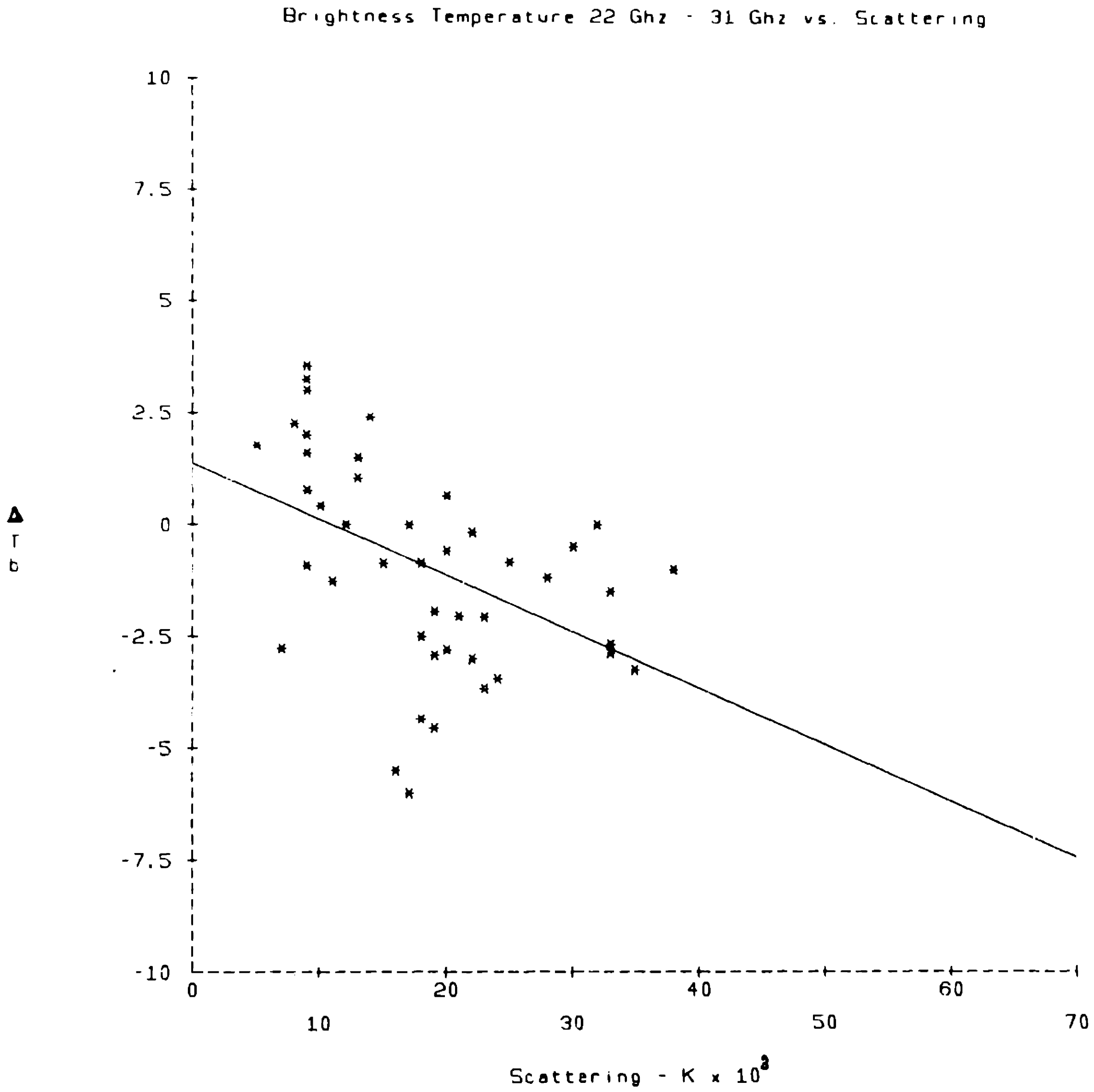

Figure 10: $T_{b22}-T_{b31}$ for Antarctica in November. Solid line is the least squares fit to the data. (Scattering is K x 10^3).

latitudes from 74° to 75°S. At low levels of scattering the radiation at both frequencies probably penetrates into the negative temperature gradient region of the snow. As the scattering increases the 31 GHz. radiation does not reach to the negative temperature gradient region, and higher brightness temperatures result; the brightness temperature at 22 GHz. is still influenced by the negative gradient.

The Greenland data for November are also consistent with this theory. As can be seen in Figure 11 (datapoints from 74° to 77°N), the low scattering coefficient areas have slightly negative values of ΔT_{b22-31} for regions with higher scattering coefficients. However, in Greenland, ΔT_{b22-31} increases positively whereas it was observed to decrease in Antarctica. At this time of year the climate for Greenland is transitioning from summer to winter and the temperature gradient near the snow surface is positive. Therefore, 22 GHz. brightness temperature should increase, relative to the 31 GHz. values, with increased scattering.

The 22 GHz. coefficients which were derived from Antarctica data were not satisfactory for the Greenland analysis. Since the 31 GHz. emissivity was less influenced by sub-surface temperature gradients, these coefficients computed from Antarctica data were accurate for Greenland predictions.

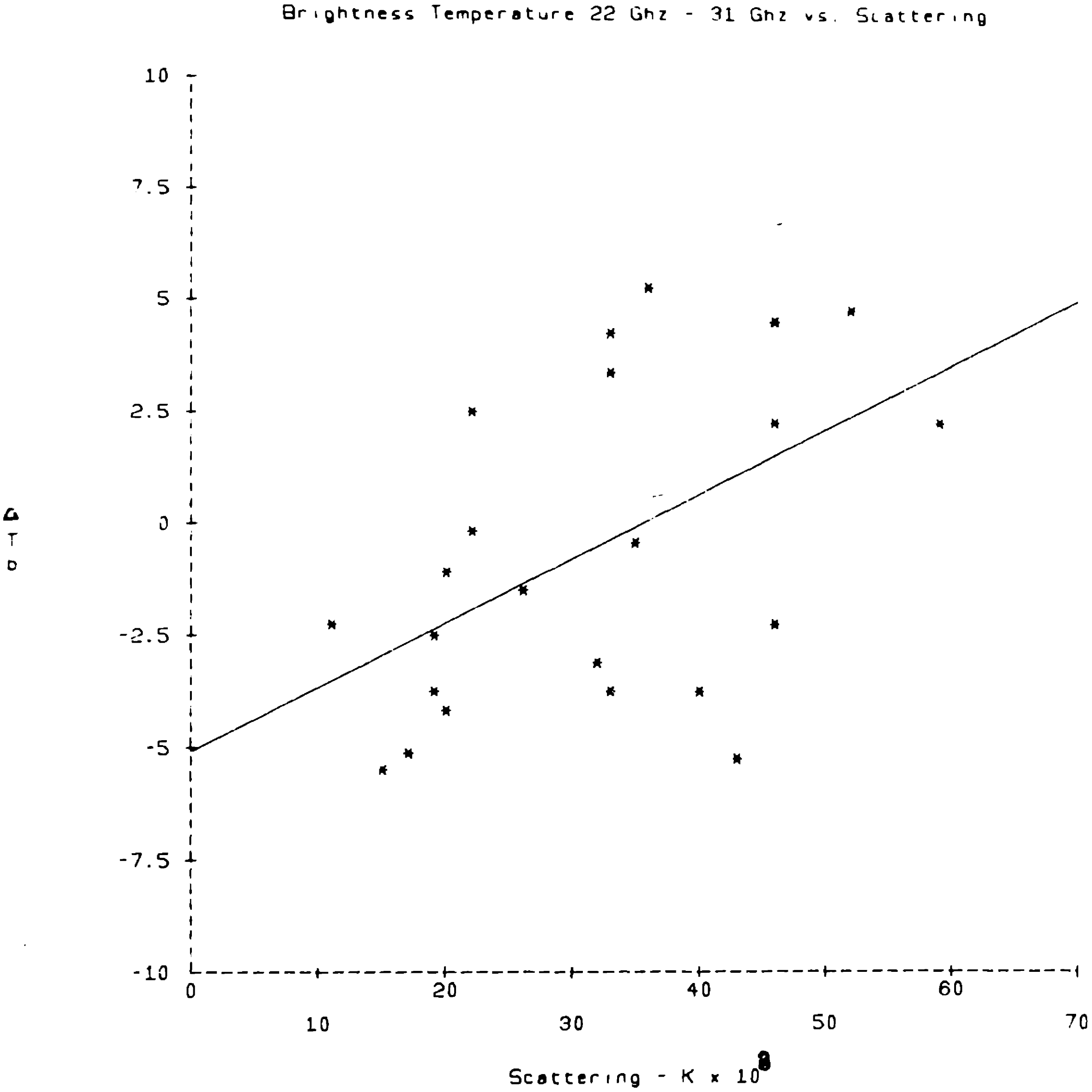

Figure 11: T_{b22}-T_{b31} for Greenland in November. Solid line is the least squares fit to the data. (Scattering is K x 10^3).

However, the gradients in the snow affect adversely the applicability of the 22 GHz. coefficients.

Near the polar regions, the exponential rate of decay of temperature with depth is expected to be less in the middle of the winter than in the summer since the cold extreme is reached earlier in the winter and lasts longer. This allows the thermal wave to penetrate deeper into the snow than for the corresponding summer gradient. Thus, the temperature gradients are not equal for summer and winter and the average microwave brightness temperature of the snow cannot be obtained by averaging the monthly readings.

This seasonal "coreless" effect varies according to latitude. Table 12 shows temperature extremes for each latitude in terms of a parameter q where, for winter,

$$T_{min} = T_{10} - qT_t \qquad (7\text{-}1)$$

and, for summer,

$$T_{max} = T_{10} + (1-q)T_t \qquad (7\text{-}2)$$

Here, T_t is the total temperature change during the year. At latitudes below 67°S (where the sun rises and sets everyday,) the snow temperature and its gradients are symmetrical for the summer and winter months and the average temperature can be obtained from the monthly averages.

The relation between the seasonal temperature gradients in the snow and changes in microwave brightness temperatures will now be investigated. The variation of snow temperature with depth will be assumed to follow the expression:

$$T(z) = T_{10}+T_1\exp(-fz) \qquad (2-1)$$

where $T(z)$ is the physical temperature, T_{10} is the ten meter temperature, f is the decay coefficient, and z is the depth in the snow.[10] For a physical temperature distribution of this form, the brightness temperature is given by:

$$T_b = \left[T_{10}\,Z\left\{\frac{K_a(T)}{\sqrt{2K}}\right\}\right] + \left[T_1\left\{\frac{K_a(T)}{K_a(T)+f}\right\}Z\left\{\frac{K_a(T)+f}{\sqrt{2K}}\right\}\right] \qquad (7-3)$$

where the first term on the right corresponds to the component of brightness temperature due to a constant term in the temperature profile (equation 5-8) and the second term to the component due to a decaying exponential (equation 5-13). The difference between the September and the January brightness temperatures will be designated D_{31} and D_{22} for 31 and 22 GHz. respectively. Designating T_1 as the difference between the September and November surface temperatures and T_2 as that betwee November and January, a modified form of equation (7-3) can be written for the seasonal difference in brightness temperature at 22 GHz which eliminates the constant term to give:

$$D_{22} = \left[T_1 \frac{K_{a22}}{K_{a22}+f_1}\right]\left[Z\left(\frac{K_{a22}+f_1}{\sqrt{2}K_{22}}\right)\right] + \left[T_2 \frac{K_{a22}}{K_{a22}+f_2}\right]\left[Z\left(\frac{K_{a22}+f_2}{\sqrt{2}K_{22}}\right)\right] \tag{7-4}$$

Here f_1 and f_2 are the thermal decay constants for September and January respectively; the temperature dependence of K_a is implicit to simplify notation. The equation for D_{31} can be written in the same form as equation 7-4 but with the subscript 22 replaced by 31.

Since our analysis assumes that the absorption coefficient K_a is proportional to ν (frequency) and the scattering coefficient K_s to ν^2, the expression for D_{31} can be written from equation 7-4 (with the appropriate changes in subscripts) as

$$D_{31} = \left[T_1 \frac{K_{a22}}{K_{a22}+vf_1}\right]\left[Z\left(\frac{K_{a22}+vf_1}{\sqrt{2}K_{22}}\right)\right] + \left[T_2 \frac{K_{a22}}{K_{a22}+vf_2}\right]\left[Z\left(\frac{K_{a22}+vf_2}{\sqrt{2}K_{22}}\right)\right] \tag{7-5}$$

where

$$v = \frac{\nu_{22}}{\nu_{31}} \approx \frac{22.2}{31.4} \approx .7$$

Dividing equation 7-4 by equation 7-5, one obtains

EFFECT OF LATITUDE ON TEMPERATURE EXTREMA

Lat	q
90	.318
80	.394
78	.409
76	,424
74	.440
72	.456
70	.472
67	.500

Table 4: The effect of latitude on the temperature swing where $T_{min}=T_{10}-qT_t$ (T_{min} is the winter temperature; T_{10} is the ten-meter temperature, and T_t is the total temperature swing between summer and winter.)

data and on the following rationale; the faster temperature changes from mid-year to summer than from mid-year to winter would be expected to lead to correspondingly larger temperature gradients (greater values of f) and coincidentally corresponds to larger temperature excursions.

Equations 7-7, 7-8, and 7-9 are next combined to give:

$$f_2 = f_1 \frac{(1-q)}{q} \tag{7-10}$$

Defining

$$q_1 = \frac{1-q}{q} \tag{7-11}$$

equation 7-6 becomes

$$\frac{D_{22}}{D_{31}} = \frac{\left[\frac{q K_{a22}}{K_{a22}+f_1}\right]\left[Z\left(\frac{K_{a22}+f_1}{\sqrt{2}K_{22}}\right)\right] + \left[\frac{(1-q) K_{a22}}{K_{a22}+q_1 f_1}\right]\left[Z\left(\frac{K_{a22}+q_1 f_1}{\sqrt{2}K_{22}}\right)\right]}{\left[\frac{q K_{a22}}{K_{a22}+V f_1}\right]\left[Z\left(\frac{K_{a22}+V f_1}{\sqrt{2}K_{22}}\right)\right] + \left[\frac{(1-q) K_{a22}}{K_{a22}+q_1 \cdot V \cdot f_1}\right]\left[Z\left(\frac{K_{a22}+q_1 V f_1}{\sqrt{2}K_{22}}\right)\right]} \tag{7-12}$$

Equation 7-12 is complicated but contains only one parameter (f_1) which was not previously determined by our analysis. Thus, the value of the thermal decay coefficient f_1 may be calculated from the brightness temperatures at 22 and 31 GHz. at both seasonal extremes. The geographical latitude, the ten meter temperature, and the emissivity are also implicity used in this calculation through q, K_a, and K (equations 7-7, 5-15, and 5-8 respectively.)

This approach has two principal difficulties. First, the seasonal surface temperature changes have not been measured accurately in many locations. Second, the operating frequencies are too close together for accurate dual-frequency measurements. A wider range of frequencies (such as those available from the SMMR experiment scheduled for the Nimbus-7 flight to be launched in September, 1978) would provide greater resolution.

It is interesting to note that not all values of D_{22}/D_{31} are reasonable. Since the 22 GHz. waves penetrate deeper than 31 GHz. into the snow (where changes of physical temperature are less than those at the surface), the change in the brightness temperature at 22 GHz. should be generally less than that at 31 GHz. Equation 7-12 can be used to demonstrate the physically obvious result that as f_1 approaches zero, D_{22}/D_{31} approaches unity. Moreover as f_1 approaches infinity (corresponding to large thermal gradients near the snow surface), the lower limit of D_{22}/D_{31} is ν_{22}/ν_{31} or approximately .7. Assuming an exponential model, the ratio of seasonal brightness temperature variations for the two radiometers D_{22}/D_{31} must therefore lie within the range of .7 to 1.0, irrespective of the temperature gradients in the snow. These limits were obeyed for seventy per cent of our three hundred point Antarctic dataset. Ten per cent were too high (D_{22} greater than D_{31}) and twenty per cent were too low. Pragmatically, f_1 was assumed equal to zero for those ratios above the limit and to ten for ratios below.

Maps 21 and 22 show geographical contours for the thermal decay depth $(f_1)^{-1}$ in both Antarctica and Greenland, which were derived from the previous analysis. A few trends are immediately noticeable. First, the areas of low and high values of f_1 cluster geographically. In Antarctica, geographical areas with large temperature gradients are evident at 120°E, 30°E and at 90°W. Small temperature gradients occur near 80°E and 130°W. In Greenland, temperature changes penetrate deeper in the 77°-79°N latitude areas than at lower latitudes.

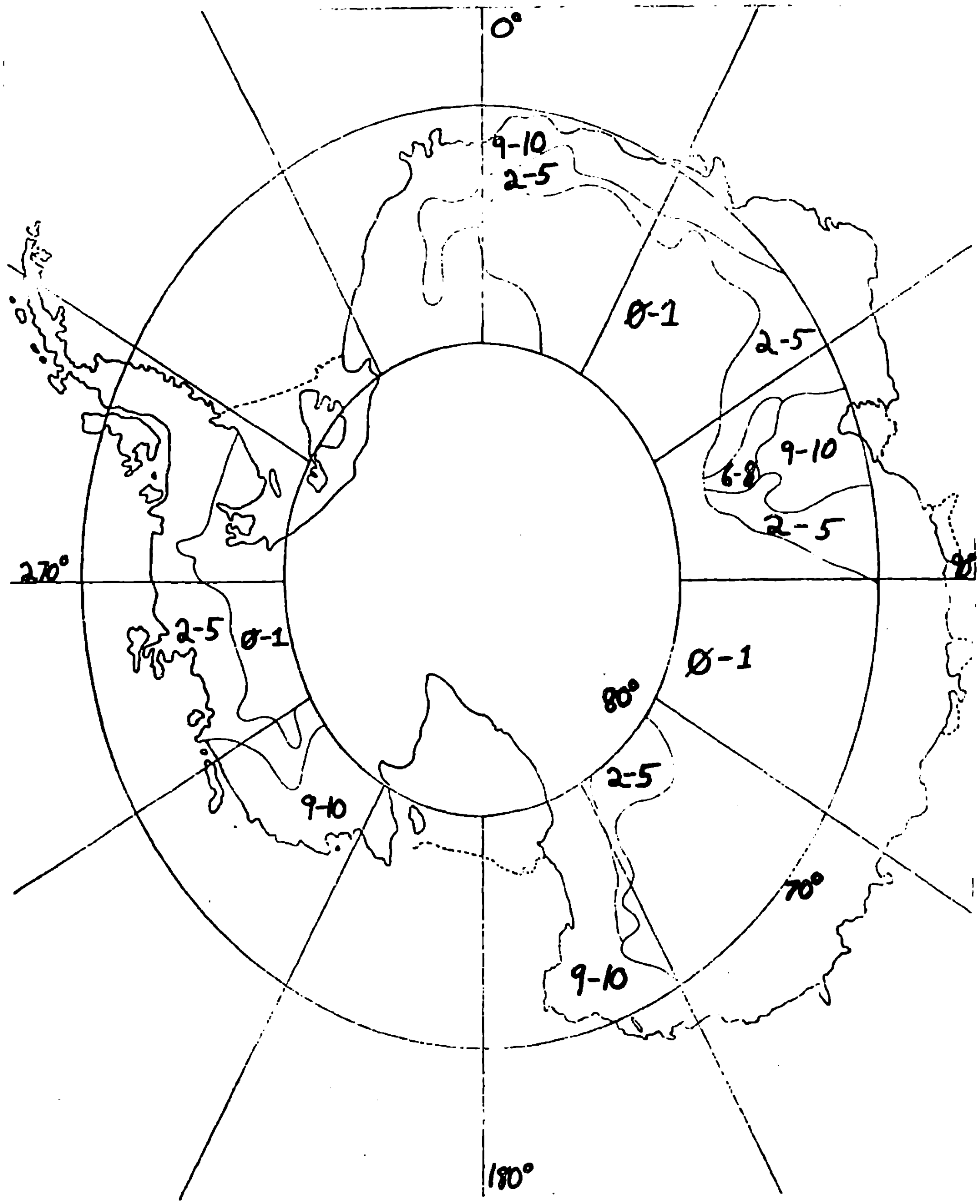

Map 21: Depth of penetration of the thermal gradient for Antarctica at the seasonal extremes. Depths are measured in meters.

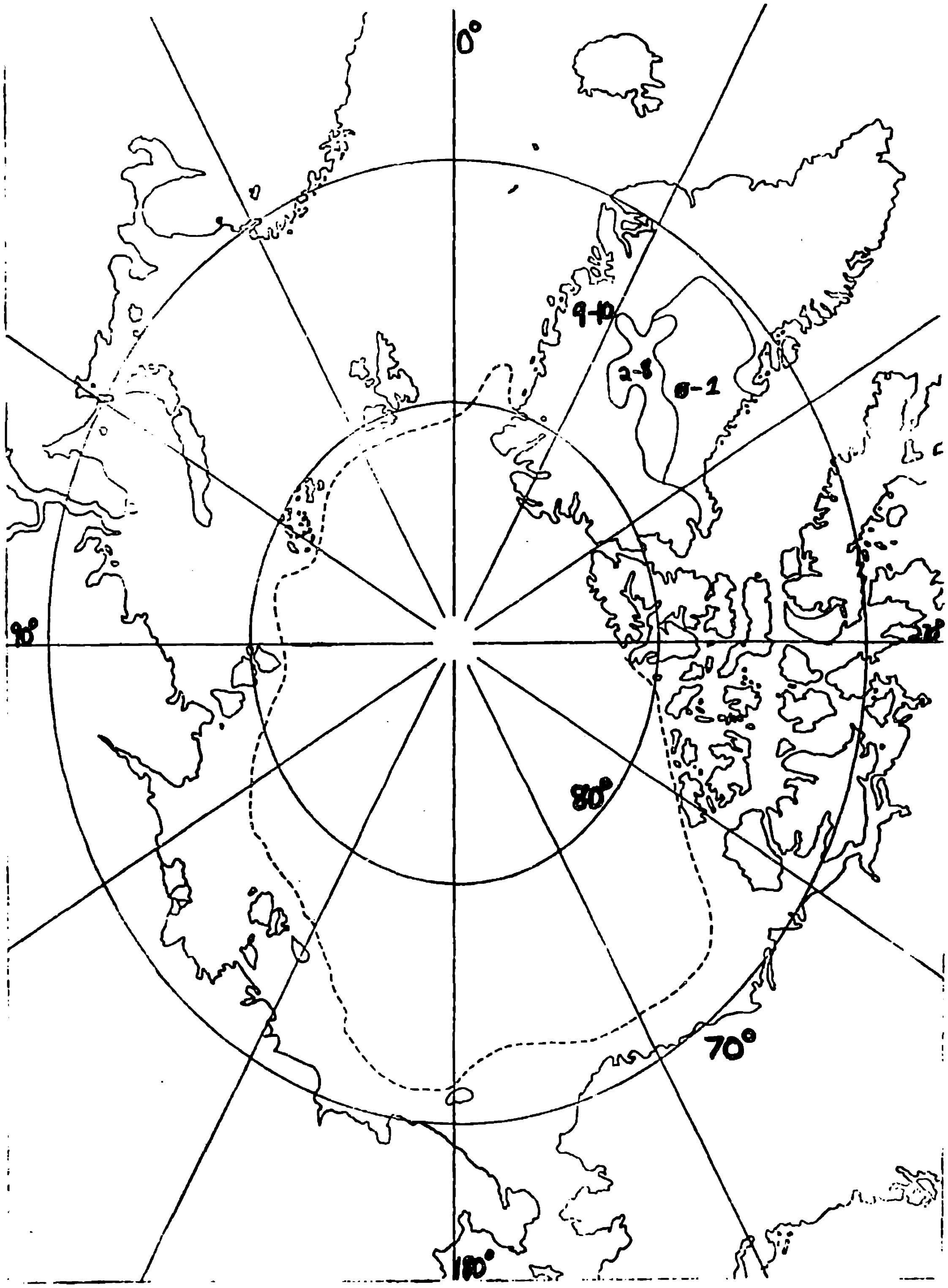

Map 22: Depth of penetration of the thermal gradient for Greenland at the seasonal extremes. Depths are measured in meters.

In regions with similar surface temperatures, a high snow accumulation rate is associated with larger temperature gradients. This observation is physically defensible since higher accumulation would result in powdery snow with low thermal conductivity in the top few meters. In addition, in regions of similar snow accumulation, higher temperatures are related to lower thermal gradients; this is consistent with physical intuition since thermal conductivity in snow generally increases with physical temperature. However, neither of these trends is strong enough to completely account for the geographical distribution of the thermal character of the snow.

CHAPTER 8 -- SUMMARY AND CONCLUSIONS

With automatic pattern recognition techniques, the microwave signatures of ice and snow surfaces at seven angles, including nadir, have been observed at two frequencies (22.2 and 31.6 GHz). For both the polar regions characteristic curves for firn sea-ice and water have been examined; results indicate that valuable information is contained in the angular changes in the brightness temperatures. The emissivity is definitely not isotropic; based in part on the angular emissivity, separate classes have been distinguished for snow-covered sea-ice and firn.

A theoretical equation relating the accumulation, temperature, and emissivity of snow has been derived and used to generate accumulation maps.which show good correlation and possibly even an improvement over those obtained previously by ground measurements. Further studies evaluated the differences between 22 GHz, and 31 GHz. for the November data and observed the temperature changes between the seasons. The differences between the brightness temperatures at the two frequencies seem to be related to temperature gradients in the snow and to vary between summer and winter in a logical manner. The available groundtruth and satellite observations of brightness temperatures were utilized to infer the snow temperature gradient at a variety of locations.

With the advantage of being able to scan areas inaccessible to man, passive microwave radiometry can detect the accumulation rate and other physical parameters of dry snow in Greenland and the Antarctic. Our analysis indicates that the use of two microwave frequencies can yield profiles of temperature and scattering beneath the snow's surface.[23] However, the present analysis is limited by the narrow range of frequencies which were used in the Nimbus-6 experiments. It is expected that the Nimbus-7 radiometers, with five useable frequencies at 7, 10, 18, 21, and 37 GHz, would provide much greater resolution of both dry and wet snow parameters and enable the evaluation of the relative merits of a layered versus a particle-scattering model for the snow.

Finally this paper has used an empirical approach based on a simple one-flux radiative transfer model and single particle scattering. It has not rigorously considered more complex models [5,6,7] which may offer a higher degree of precision. Our essential aim in this paper, as in previous papers,[22] was to provide a preliminary analysis of the wealth of snow and ice data from the SCAMS experiment. It is our hope that this data base may serve as input for further evaluation.

FOOTNOTES

1. Kunzi, K. F., A.D. Fisher, and D.H. Staelin, "Snow and Ice Surfaces Measured by the Nimbus Microwave Spectrometer", *Journal of Geophysical Research*, Vol. 81, No. 27, 1976, pp. 4965-4980.

2. Chang, T.C., P. Gloersen, T. Schmugge, T.T. Wilheit, and H.J. Zwally, "Microwave Emission from Snow and Glacier Ice", *Journal of Glaciology*, Vol. 16, No. 74, 1976, pp. 223-239.

3. Zwally, H.J., "Microwave Emissivity and Accumulation Rate of Polar Firn", *Journal of Glaciology*, Vol. 18, No. 79, 1977, pp. 195-215.

4. Fisher, A.D., "Models for Scattering in an Inhomogeneous Medium", internal report, May, 1975.

5. Fisher, A.D., "A Model for Microwave Intensity Propagation in an Inhomogeneous Medium", *IEEE Transactions on Antennas and Propagation*, Vol AP-25, No. 6, November, 1977, pp. 876-882.

6. Tsang, L. and J. A. Kong, "Thermal Microwave Emission from Half-space Random Media", *Radio Science*, Vol. 11, No. 7, 1976, pp. 599-609.

7. Tsang, L. and J.A. Kong, "The Brightness Temperature of a Half-space Random Medium with Nonuniform Temperature Profile", *Radio Science*, Vol. 10, No. 12, 1975, pp. 102 1033.

8. Staelin, D.H., A.H. Barrett, P.W. Rosenkrantz, F.T. Barath, E.J. Johnson, J.W. Waters, A.Wouters, and W.B. Lenoir, "The Scanning Microwave Spectrometer (SCAMS) Experiment *The Nimbus-6 Users Guide*, Greenbelt, Goddard Space Flight Center, 1975, pp. 59-86.

9. Staelin, D.H., "Passive Remote Sensing at Microwave Wavelengths", Proceedings of the IEEE, Vol 57, No. 4, April, 1969, pp. 427-439.

10. Bentley, C.R., R.L. Cameron, C. Bull, K. Kojima, and A.J. Gow, "Physical Characteristics of the Antarctic Ice Sheet", Antarctic Map Folio Series, Folio 2, 1962, pp. 1-10.

11. Fristrup, B., "The Greenland Ice Cap", University of Washington Press, Rhodos, Copenhagen, 1966, p. 234 and p. 230.

12. Lettau, H., "Antarctic Atmosphere as a Test Tube for Meteorological Theories", Research in the Antarctic, edited by Louis Quam, American Association for the Advancement of Science, 1971, pp. 429-442.

13. Moran, J.M., "Radiometric Observation of the Moon Near 1 cm. Wavelength", M.S. Thesis at Massachusetts Institute of Technology, June, 1965.

14. Bull, C., "Snow Accumulation in Antarctica", Research in the Antarctic, edited by Louis Quam, American Association for the Advancement of Science, 1971, pp. 367-421.

15. Nagy, G., "State of the Art in Pattern Recognition", Proceedings of the IEEE, Vol. 56, No. 5, 1968, pp. 836-862.

16. Anderberg, M.R., Cluster Analysis for Applications, New York, Academic Press, 1973.

17. Duda, R.O. and Hurt, P.E., "Pattern Classification and Scene Analysis, New York, John Wiley, 1973.

18. Gloersen, P., T.T. Wilheit, T.C. Chang, W. Nordbert, and W.J. Campbell, "Microwave Maps of the Polar Ice of the Earth", Bulletin of the American Meteorological Society, Vol. 55, No. 12, pp. 1442-1448.

19. Edgerton, A.T., R. Ruskey, D. Williams, A. Stogryn, G. Poe, D. Meeks, and O. Russel, "Microwave Emission Characteristics of Natural Materials and the Environment", United States Technical Report AD720388, February, 1971.

20. Abromowitz, M. and I.A. Stegum, "Handbook of Mathematical Functions", National Bureau of Standards, Applied Math Series, No. 55, p. 299.

21. Gow, A.J., "On the Rates of Growth of Grains and Crystals in South Polar Firn", Journal of Glaciology, Vol. 8, No. 53, 1969, pp. 241-252.

22. Fisher, A.D., B.L. Ledsham, P.W. Rosenkrantz, and D.H. Staelin, "Satellite Observations of Snow and Ice with an Imaging Passive Microwave Spectrometer", Proceedings of Symposium on Meteorological Observations from Space, pp. 98-103, 1976.

23. Fisher, A.D., S.R. Rotman, and D.H. Staelin, "An Analysis of Microwave Remote Sensing Data by Pattern Recognition Techniques", presented at URSI Meeting, Boulder, Colorado, January, 1978.